Calcium signals tune AMPK activity and mitochondrial homeostasis in dendrites of developing neurons

Condensed title: Ca^{2+}-AMPK tunes mitochondria in dendrites

Akane Hatsuda[1,2], Junko Kurisu[2], Kazuto Fujishima[2,†], Ayano Kawaguchi[3,4], Nobuhiko Ohno[5,6], Mineko Kengaku[1,2]

1. Graduate School of Biostudies, Kyoto University, Japan
2. Institute for Integrated Cell-Material Sciences (KUIAS-iCeMS), Kyoto University, Japan
3. Department of Anatomy and Cell Biology, Nagoya University Graduate School of Medicine, Japan
4. Department of Human Morphology, Okayama University Graduate School of Medicine, Density and Pharmaceutical Sciences, Japan.
5. Department of Anatomy, Division of Histology and Cell Biology, Jichi Medical University, Japan
6. Division of Ultrastructural Research, National Institute for Physiological Sciences, Japan

Corresponding authors. Email: kengaku@icems.kyoto-u.ac.jp

†Present address: Department of Anatomy and Cell Biology, Division of Life Sciences, Osaka Medical and Pharmaceutical University, Japan

Abstract

AMP-activated protein kinase (AMPK) governs multiple pathways regulating mitochondrial dynamics and homeostasis. AMPK overactivation is a hallmark of some neurodegenerative diseases, leading to excessive mitochondrial fission and mitophagy and subsequent degeneration of neuronal processes. Here we demonstrate that AMPK is involved in activity-dependent dendritic outgrowth of developing hippocampal neurons. AMPK deficiency phenocopies the inhibition of neuronal activity, inducing dendritic hypotrophy with abnormally elongated mitochondria. In growing dendrites, AMPK is activated by neuronal activity and dynamically oscillates in synchrony with calcium spikes, and this AMPK oscillation is inhibited by CaMKK2 knockdown. AMPK activation leads to phosphorylation of MFF and ULK1, which initiate mitochondrial fission and mitophagy, respectively. Dendritic mitochondria in AMPK-depleted neurons exhibit impaired fission and mitophagy and display multiple signs of dysfunction. Thus, AMPK activity is finely tuned by the calcium-CaMKK2 pathway and regulates mitochondrial homeostasis by facilitating removal of damaged components in rapidly growing neurons during normal brain development.

Introduction

Dendrite morphogenesis is a pivotal step for the establishment of neural circuit connectivity in the developing brain. Rapid extension and branching of dendrites in developing neurons is accompanied by extensive cytoskeletal and membrane remodeling and intracellular transport that increase the energetic burden particularly in growing dendritic branches. We have previously shown that mitochondria are actively transported to growing dendritic arbors to maintain local ATP levels necessary for the regulation of actin dynamics[1]. In addition to producing the majority of cellular ATP, mitochondria also participate in various processes indispensable for the development and function of dendrites, including Ca^{2+} homeostasis, lipid flux, and reactive oxygen species (ROS) generation[2,3]. The abnormal morphology of dendritic mitochondria is one of the pathogenic hallmarks of Alzheimer's disease (AD), supporting the notion that constant delivery of functional mitochondria throughout a large volume of dendrites is critical for maintenance as well as differentiation of neurons[4,5].

Mitochondrial homeostasis in postmitotic neurons is highly dependent on dynamic fission and fusion events. Mitochondrial fission is particularly important for the biogenesis of new mitochondria and for the removal of damaged or aged mitochondria through mitophagy[6]. Mitochondrial fission is triggered by the spiral assembly of an evolutionally conserved GTPase dynamin-related protein 1 (Drp1) around the constriction site on the mitochondrial surface. During fission, Drp1 is recruited to the outer mitochondrial membrane by one of its receptors, such as Mitochondrial Fission Factor (MFF)[7–9]. Several groups, including us, have shown that the inhibition of mitochondrial fission leads to abnormal elongation and dysfunction of mitochondria, resulting in aberrant dendrite formation in vivo and in vitro[10–12]. On the other hand, excessive mitochondrial fission also leads to reduced respiratory activity and abnormal distribution of mitochondria, which impairs normal development of dendrites[13,14]. However, it remains unclear how the proper balance of mitochondrial fission is adaptively regulated in developing neurons whose shape, volume and activity states are dynamically changing.

The balance between fission and fusion should be finely tuned in response to changes in the cellular and subcellular metabolic state. Recent studies have highlighted the role of AMP-activated protein kinase (AMPK) as an energy sensor that sustains the metabolic state by regulating mitochondrial dynamics and functions[15]. AMPK regulates several aspects of mitochondrial homeostasis by direct phosphorylation of key factors, including MFF, peroxisome proliferator-activated receptor-coactivator 1 (PGC1α), Armadillo repeat-containing protein 10 (ARMC10), Unc-51 like autophagy activating kinases 1 and 2 (ULK1/2) and Mitochondrial

fission regulator 1-like protein (MTFR1L)[16–22]. AMPK is activated by direct allosteric binding of AMP, facilitating phosphorylation at Thr172 by an upstream kinase LKB1 in response to cellular ATP shortage[23]. Additionally, AMPK can be directly phosphorylated by the calcium (Ca^{2+})-sensitive kinase CaMKK2 (also known as CaMKKβ) in response to an elevated intracellular Ca^{2+} concentration[24,25]. In the central nervous system, overactivation of the CaMKK2-AMPK pathway by excessive Ca^{2+} signals has been implicated in mitochondrial fragmentation and degradation during the pathogenesis of Alzheimer's disease[26,27].

It is widely accepted that Ca^{2+} signals evoked by neuronal activity play important roles in dendrite development. Ca^{2+} influx via voltage-gated calcium channels (VGCCs) and NMDA receptors triggers activation of Ca^{2+}/calmodulin-dependent kinases (CaMKs) that positively and negatively regulate dendrite growth through transcriptional control and local remodeling of the cytoskeleton[28–30]. In mature neurons, activity-induced Ca^{2+} signals have been shown to induce mitochondrial fission in dendrites[10,31]. However, the causal link between Ca^{2+} signals evoked by neuronal activity and mitochondrial fission is less understood in the growing dendrites of developing neurons. In this study, we investigated the impact of neuronal activity on the dynamics of dendritic mitochondria in differentiating hippocampal neurons. We demonstrate that neuronal activity finely tunes the CaMKK2-AMPK pathway in growing dendrites. Normal AMPK activity induces mitochondrial fission and mitophagy via phosphorylation of MFF and ULK1, which are critical to remove dysfunctional mitochondrial components and maintain functional mitochondria in growing dendrites. Thus, there is indeed a causal link between activity-dependent dendritic arbor development and AMPK-dependent mitochondrial quality control.

Results

Neuronal activity enhances dendrite formation and mitochondrial fission in developing hippocampal neurons

We previously established long-term live-imaging of dissociated hippocampal neurons and observed the gradual formation of dendritic arbors, with dynamic extension and retraction, until the second week of culture[32]. To visualize neuronal activity in developing dendrites, we transfected GCaMP6s in cultured hippocampal neurons and performed live imaging at 5 days in vitro (DIV5). We observed intermittent Ca^{2+} transients in dendrites and cell soma, which were abolished by the combined treatment with a blocker of voltage-gated sodium channels, tetrodotoxin, and an NMDA receptor antagonist, D-(-)-2-Amino-5-phosphonopentanoic acid (TTX+APV treatment) (Fig. 1A, Supplementary Video 1). There was no apparent difference in the dynamic extension and retraction of dendrites in drug-treated and untreated neurons, but growth retardation gradually became evident, with a significant decrease in total dendritic length and the number of branches at 48 hr after TTX+APV treatment (Fig. 1B-D, Supplementary Video 2).

To examine if neuronal activity affects mitochondrial dynamics in growing dendrites, we transfected Mito-DsRed into neurons that were then untreated or treated with TTX+APV. Under both conditions, mitochondria were distributed throughout the dendritic arbors, and a significant fraction of them moved along the dendritic shaft as previously reported by us and others[1,33–35]. Inhibition of neuronal activity did not affect mitochondrial motility in dendrites: neither the fraction of motile mitochondria nor their average speed was altered by TTX+APV treatment (Extended Data Fig. 1A and B). There were no apparent changes in the density and distribution of mitochondria in dendrites in the drug-treated neurons (Extended Data Fig. 1C). However, we found a significant increase in the length of dendritic mitochondria in the drug-treated neurons [Median (IQR)= 2.0 (1.2- 2.9) μm in control vs 2.5 (1.6-3.8) μm in TTX+APV neurons; Fig. 1E, G, H, I]. In the axon, on the other hand, the length of mitochondria was much shorter, as previously reported[36], and was unaffected by TTX+APV treatment (Fig. 1F). As mitochondrial morphology is affected by the balance between fission and fusion, we analyzed the frequency of fission and fusion in dendrites by high resolution time-lapse imaging (Extended Data Fig. 1D and Supplementary Video 3). We found that inhibition of neuronal activity significantly suppressed mitochondrial fission but had little or no effect on fusion (Fig. 1J). Conversely, glutamate treatment led to a marked increase in smaller mitochondria in the cell soma and

125 dendrites, suggesting that enhanced neuronal activity facilitated mitochondrial fission (Extended
126 Data Fig. 1E). Taken together, these data suggest that neuronal activity is involved in the
127 regulation of the mitochondrial fission-fusion balance during dendritic outgrowth in developing
128 neurons.
129
130 **AMPK regulates dendritic growth and mitochondrial fission**
131 It has been shown that AMPK mediates mitochondrial fission in response to energy stress in
132 neurons and non-neuronal cells[17]. We therefore examined if AMPK is involved in activity-
133 dependent mitochondrial fission in developing hippocampal neurons. AMPK is a heterotrimeric
134 serine/threonine kinase composed of one catalytic (α1/α2), one regulatory (β1/β2) and one
135 AMP/ATP binding (γ1/γ2/γ3) subunit. Both AMPKα1 and AMPKα2 were expressed in cultured
136 hippocampal neurons, as assessed by western blotting using isoform-specific antibodies (Fig. 2A).
137 Specifically, AMPKα1 expression was high in earlier stages and declined by DIV10, whereas
138 AMPKα2 expression started at a level comparable to AMPKα1, and then gradually increased,
139 peaking at DIV10. The abundance of active AMPKα phosphorylated at Thr172 (detected by an
140 antibody that recognizes both phosphorylated isoforms, p-AMPKα) increased during dendritic
141 outgrowth in parallel with AMPKα2 expression (Fig. 2A).
142 To investigate the role of AMPK in mitochondrial dynamics and dendritic formation,
143 we knocked down AMPK subunits in cultured neurons by expressing short hairpin RNAs
144 (shRNA) against AMPKα1 and AMPKα2 (Extended Data Fig. 2A and B). At DIV3, we
145 transfected dissociated hippocampal neurons with AMPKα1 shRNA or AMPKα2 shRNA
146 plasmids together with a volume marker GFP construct, and observed dendritic morphology at
147 DIV5. AMPKα2 shRNA significantly reduced the size and complexity of dendritic branches,
148 reminiscent of the activity-deprived neurons (Fig. 2B-D and Extended Data Fig. 2C-E compared
149 to Fig. 1). Concomitant exogenous expression of an AMPKα2 mutant cDNA (AMPKα2 Rescue)
150 that was resistant to AMPKα2 shRNA largely prevented the dendritic defects, discounting any
151 major off-target effects of the shRNA (Fig. 2B-D and Extended Data Fig. 2C). In contrast,
152 AMPKα1 shRNA produced much weaker effects on dendritic morphology. Further, simultaneous
153 knockdown of AMPKα1 and α2 was not phenotypically different from AMPKα2 knockdown,
154 suggesting that AMPKα2 was the predominant isoform regulating dendritic morphogenesis in
155 our culture (Extended Data Fig. 2C-E). We further confirmed that repression of AMPKα2 using
156 CRISPR interference (CRISPRi) significantly delayed dendritic outgrowth at DIV5 (Extended
157 Data Fig. 2F-H). We thus focused on AMPKα2 in subsequent experiments.

158 To confirm the requirement of AMPKα2 for dendritic formation in vivo, we introduced
159 the AMPKα2 shRNA#1 together with GFP into CA1 pyramidal neurons at embryonic day (E)
160 14.5 by in utero electroporation. Compared to control neurons, AMPKα2-depleted neurons
161 showed significantly reduced length and complexity of the apical dendrite at P5, supporting the
162 notion that AMPKα2 functions in dendritic outgrowth of hippocampal pyramidal neurons (Fig.
163 2E-H). In contrast, the dendritic hypotrophy was less evident at P10, suggesting a compensatory
164 mechanism allows the recovery of dendritic growth retardation in the context of AMPKα2
165 deficiency in vivo.
166 Returning to cultured cells, we next observed mitochondria in AMPKα2-depleted
167 neurons by cotransfecting mito-DsRed and GFP. The AMPKα2 knockdown significantly
168 increased mitochondrial length in dendrites [Median (IQR)= 2.1 (1.3-3.1) μm in control; 2.6 (1.6-
169 4.1) μm in AMPKα2 knockdown; 2.0 (1.3-3.1) μm in rescue; Fig. 3A, C-E], but not in the axon
170 at DIV5 (Fig. 3B). There was no apparent change in the density and distribution of mitochondria
171 in the hypotrophic dendrites in AMPKα2-depleted neurons (Extended Data Fig. 3A). AMPKα2
172 CRISPRi also induced abnormal elongation of mitochondria in dendrites (Extended Data Fig. 3B-
173 E). These results prompted us to use time-lapse imaging to analyze the fission/fusion frequency
174 of dendritic mitochondria in the neurons transfected with AMPKα2 shRNA. As in the case for
175 neuronal activity inhibition, AMPKα2 knockdown specifically lowered the frequency of fission
176 but had little effect on fusion in dendrites (Fig. 3F).
177 We further documented the importance of AMPK activity in mitochondrial dynamics
178 by pharmacological activation and inhibition. We found that dendritic mitochondria were
179 significantly shortened after a 3-5 h treatment with an AMPK activator, AICAR (1 mM) (Fig. 3G-
180 J). In contrast, treatment with an AMPK inhibitor, Compound C (20 μM), elongated dendritic
181 mitochondria (Fig. 3K-N), underscoring the involvement of AMPK in the regulation of
182 mitochondrial fission in hippocampal neurons. Collectively, these data suggest that AMPKα2 has
183 critical roles in mitochondrial fission and dendritic formation in hippocampal neurons, and that
184 the two phenomena are mechanistically linked.
185
186 **Neuronal activity induces dynamic oscillation of AMPK activity via Ca/CaMKK2**
187 The striking phenotypic similarities between the modulation of neuronal activity and AMPK
188 activity prompted us to examine if AMPK mediates the activity-dependent control of
189 mitochondrial dynamics in developing dendrites. In order to analyze the spatiotemporal dynamics
190 of AMPK activity in developing hippocampal neurons, we transfected them with AMPKAR-EV,

191 a highly sensitive fluorescence resonance energy transfer (FRET)-based biosensor for AMPK[37].
192 We observed high basal FRET signals in the axon, which presumably reflected the activity of
193 AMPK-related kinases such as SAD-A/B[38–40]. Indeed, AMPKα2 shRNA specifically suppressed
194 FRET signals in the somatodendritic compartment but not in the axon (Extended Data Fig. 4A),
195 supporting the notion that the FRET signals in dendrites, but not in axons, reflect AMPK activity.
196 Consistent with previous reports, we observed a rapid increase in AMPK activity in
197 the cell body and dendrites upon glutamate treatment[41,42]; moreover, the AMPK activity was
198 abrogated by AMPKα2 knockdown (Extended Data Fig. 4B). Interestingly, we found an
199 unambiguous periodic fluctuation of AMPK activity with a frequency of 0 to 4 peaks in 3 minutes,
200 in the somatodendritic compartment of untreated neurons (Fig. 4A and C). The basal fluctuation
201 was suppressed by cotransfection of AMPKα2 shRNA or inhibition of neuronal activity by
202 TTX+APV treatment, suggesting that neuronal activity caused dynamic changes in AMPK
203 activity (Fig. 4A-D). To further prove the causal relationship of neuronal activity and AMPK
204 activation, we performed simultaneous imaging of Ca^{2+} and AMPK activity using a red
205 fluorescent Ca^{2+} indicator, jRGECO1a, together with AMPKAR-EV. We observed periodic Ca^{2+}
206 spikes which highly synchronized with AMPK activity fluctuation in dendrites (Fig. 4E, F and
207 Supplementary Video 4). The temporal cross-correlation analysis revealed the highest correlation
208 at 5 sec after Ca^{2+} influx, indicating that Ca^{2+} influx precedes AMPK activation (Fig. 4G).
209 Inhibition of neuronal activity by TTX+APV treatment suppressed both Ca^{2+} spikes and AMPK
210 fluctuation (Extended Data Fig. 4C). In contrast, AMPK knockdown suppressed only the AMPK
211 fluctuation, and did not alter the Ca^{2+} transient (Extended Data Fig. 4D), indicating that AMPK
212 fluctuation was induced by neuronal activity.
213 Two upstream kinases, CaMKK2 and LKB1, regulate AMPK activity by
214 phosphorylation[23–25]. As CaMKK2 has been implicated in activity-dependent formation of
215 dendrites[43,44], we examined whether CaMKK2 is required for AMPK fluctuation in response to
216 neuronal activity. Cotransfection of CaMKK2 shRNA or treatment with CaMKK2 inhibitor
217 (STO609, 10 μM) suppressed the periodic activation of AMPK (Fig. 4H-J). On the other hand,
218 the AMPK fluctuation was not affected by treatment with an LKB1 inhibitor (Pim1, 1μM)
219 Extended Data Fig. 4E).
220 Taken together, these data suggest that neuronal activity dynamically regulates AMPK
221 activity via Ca^{2+}/CaMKK2 in the somatodendritic region of developing hippocampal neurons.
222
223 **AMPKα2 knockdown prevents asymmetric mitochondrial fission and mitophagy in**

224 **developing dendrites**

225 Mitochondrial fission is involved in biogenesis and mitophagic degradation of mitochondria. It
226 has recently been reported that the downstream pathways could be distinguished by the position
227 of fission, either at the midzone or the periphery[45]. In normal developing hippocampal neurons,
228 we observed both midzone and peripheral fissions in growing dendrites, with the frequency of the
229 midzone fission, which was implicated in mitochondrial biogenesis in the previous study[45], being
230 approximately 2.1-fold higher than peripheral fission (Fig. 5A and B). TTX+APV treatment
231 hampered both midzone and peripheral fissions, but had a stronger inhibitory effect on peripheral
232 fission (Fig. 5B). AMPKα2 knockdown displayed strikingly similar effects, with stronger
233 suppression of the peripheral fission (Fig. 5C).

234 As the peripheral fission has been implicated in the mitophagy pathway, we asked
235 whether AMPK-induced mitochondrial fission is required for mitophagic degradation of dendritic
236 mitochondria. To this end, we used an antibody against the autophagy marker p62 to immunostain
237 neurons transfected with Mito-DsRed with or without AMPKα2 shRNA. The p62 signals formed
238 puncta, some of which were colocalized with mitochondria in the soma and dendrites in control
239 neurons. By contrast, the number of p62 puncta and those colocalized with mitochondria were
240 significantly decreased in AMPKα2 knockdown cells (Fig. 5D-G). These data suggest that
241 AMPK-mediated mitochondrial fission is important for the mitophagy initiation during dendrite
242 development.

243 We also examined the effect of AMPK activation on mitochondrial biogenesis. AMPK
244 has been shown to phosphorylate and activate PGC1α, the master regulator of mitochondrial
245 biogenesis. However, we detected no obvious difference in the phosphorylation level of PGC1α
246 by Phos-tag SDS-PAGE, nor the expression of PGC1α, in response to TTX+APV, Glutamate,
247 Compound C or AICAR (Extended Data Fig. 5A).

248

249 **AMPK phosphorylates mitochondrial fission factor and ULK1 in response to neuronal**
250 **activity.**

251 AMPK phosphorylates various downstream substrates involved in many aspects of mitochondrial
252 homeostasis. AMPK regulates mitochondrial fission by direct phosphorylation of MFF, which
253 promotes its association with Drp1 at the mitochondrial outer membrane[16,17]. AMPK is also
254 known to directly phosphorylate the autophagy initiating kinase ULK1[20]. We thus asked whether
255 AMPK phosphorylates these substrates in response to neuronal activity.

256 Consistent with our observation that AMPK activity was dynamically regulated in

257 synchrony with neuronal activity, AMPK phosphorylation rapidly increased within 5 min of
258 glutamate treatment (Fig. 6A). In contrast, TTX+APV treatment reduced the basal level of AMPK
259 phosphorylation. Concomitantly, MFF phosphorylation at Ser146 was increased by glutamate
260 treatment, while it was repressed by TTX+APV treatment. Likewise, the level of ULK1
261 phosphorylation at Ser555 paralleled that of AMPK phosphorylation, which was altered by
262 manipulation of the activity states in cultured neurons. We also confirmed that the
263 phosphorylation levels of MFF and ULK1 were upregulated by AICAR treatment, while they
264 were downregulated by Compound C treatment. Taken together, these results suggest that AMPK
265 activation by neuronal activity induces mitochondrial fission and mitophagy by direct
266 phosphorylation of MFF and ULK1.
267
268 **AMPK knockdown compromises normal mitochondrial activity in developing dendrites**
269 We next asked if AMPK-mediated mitochondrial fission and mitophagy is required for
270 mitochondrial quality control. Using the fluorescent dye tetramethylrhodamine methyl ester
271 (TMRM, 20 nM), we asked whether the mitochondrial membrane potential ($\Delta\Psi m$) was affected
272 in the elongated dendritic mitochondria in neurons that were defective in AMPK-mediated
273 mitochondrial fission. At first, we were unable to detect a significant difference in the average
274 intensity of basal TMRM fluorescence in individual mitochondria of control and AMPKα2
275 knockdown cells (Extended Data Fig. 5B and C). We then analyzed dynamic changes in $\Delta\Psi m$ by
276 time-lapse imaging. We observed intermittent flickers of TMRM fluorescence in some dendritic
277 mitochondria in control neurons (Fig. 6B and Supplementary Video 5). TMRM flickering is
278 caused by the opening of the mitochondrial permeability transition pore (mPTP), an essential
279 process for maintaining mitochondrial homeostasis by preventing an overload of Ca^{2+} and
280 reactive oxygen species (ROS) in the mitochondrial matrix induced by respiration activity[46,47]. In
281 AMPKα2 knockdown neurons, the frequency of TMRM flickering was significantly reduced,
282 suggestive of lower respiratory activity of mitochondria in these cells (Fig. 6C).
283 We then analyzed mitochondrial ROS levels (mitoROS) using the fluorescent dye
284 MitoSOX (500 nM). MitoROS is a byproduct of electron transport chain activity, which is
285 increased by high respiration and triggers mPTP opening[48]. MitoSOX signals formed puncta in
286 the mitochondrial matrix, which were significantly decreased in AMPKα2 knockdown cells (Fig.
287 6D and E).
288 These results strongly suggest that AMPK-mediated mitochondrial fission and
289 mitophagy is required for the maintenance of functional mitochondria in growing dendrites of

290 hippocampal neurons.

291 **Discussion**

292 To meet the rapidly growing energy demands incurred by the extension of dendritic arbors,
293 mitochondria are actively produced and transported throughout the expanding dendritic
294 compartments. Here we demonstrate that neuronal activity regulates mitochondrial homeostasis
295 through the activation of the Ca^{2+}-CaMKK2-AMPK axis to support dendritic outgrowth in
296 developing neurons. AMPK deficiency prevented mitochondrial fission and mitophagy, leading
297 to mitochondrial dysfunction with low respiratory activity and consequent growth retardation of
298 dendrites. Our observations suggest that AMPK-dependent regulation of local mitochondrial
299 homeostasis is an important mechanism of activity-induced dendritic growth besides the well-
300 known transcription-dependent mechanism.

301 Mitochondrial fission is prerequisite for the biogenesis of mitochondria and for the
302 elimination of damaged components through the mitophagy pathway[49,50]. Recent studies have
303 demonstrated that symmetric fission generating two equal daughter mitochondria leads to
304 doubling of mitochondrial biomass, while asymmetric fission generates a smaller mitochondrion
305 that is subjected to the mitophagy pathway[45]. We observed both symmetric and asymmetric
306 fissions in growing dendrites, but the asymmetric fission was more strongly affected by the
307 inhibition of neuronal activity or AMPK. We showed that neuronal activity induces
308 phosphorylation/activation of two downstream effectors of AMPK, MFF and ULK1, which are
309 the key regulators of mitochondrial fission and mitophagy, respectively. Mitochondria with
310 defective fission and mitophagy in AMPK-depleted neurons exhibit multiple signatures of
311 mitochondrial dysfunction, such as reduced $\Delta\Psi m$ flickering and ROS production, suggesting that
312 AMPK-mediated mitochondrial fission and mitophagy is required for the maintenance of healthy
313 mitochondria in growing dendrites.

314 On the other hand, we did not obtain evidence supporting the regulation of mitochondria
315 biogenesis by activity-induced AMPK signaling, such as a change in PGC1α phosphorylation and
316 expression. Nonetheless, the total biomass of dendritic mitochondria should decrease as a
317 consequence of AMPK knockdown or neuronal activity inhibition, since the mitochondrial
318 density remains the same but the dendritic volume is substantially reduced. We will need more
319 sensitive assays to draw conclusions regarding the regulation of mitochondrial biogenesis by
320 activity-induced AMPK signaling.

321 AMPK and AMPK-related kinases are expressed in both dendrites and axons of cortical
322 neurons, but their activities seem differentially regulated in distinct subcellular compartments.
323 Previous studies have shown that the activities of SAD-A/B and NUAK1 and their upstream

324 kinase LKB1 are strongly biased in the axon and regulate axon specification and branching[39,40].
325 The SAD kinase has been shown to regulate the fission/fusion balance of mitochondria through
326 phosphorylation of tau in the axon[51,52]. In contrast, we demonstrate that AMPK overactivation
327 and suppression alters mitochondrial fission, and those changes are seen only in dendrites but not
328 in the axon (Fig. 3). The activation of AMPK in dendrites and AMPK-related kinases in the axon
329 appears to be regulated by distinct molecular mechanisms: SAD-A/B and NUAK1 have been
330 shown to be constitutively activated in the axon by LKB1. In contrast, AMPK phosphorylation
331 dynamically oscillates in dendrites, depending on Ca^{2+} influx and CaMKK2 activity, while it is
332 independent of LKB1. AMPK activity was difficult to detect in the axon due to the high basal
333 FRET signals, presumably reflecting the high activity of SAD-A/B and/or NUAK1 in the axon.
334 Nonetheless, neither neural activity nor AMPK overactivation enhanced fission of axonal
335 mitochondria, suggesting that mitochondrial dynamics and transport are differentially regulated
336 in the axon and dendrites by distinct AMPK-related kinases.

337 One interesting finding in the present study is that AMPK activity dynamically oscillates in
338 synchrony with Ca^{2+} influx triggered by neuronal activity. Ca^{2+}-dependent AMPK
339 phosphorylation is rapidly downregulated in several tens of seconds, implying a regulatory loop
340 involving a negative regulator of AMPK activity which counteracts CaMKK2-mediated
341 phosphorylation. The molecular pathway of AMPK dephosphorylation is less understood, but a
342 Ca^{2+}-dependent phosphatase such as PP2A is a likely candidate, as PP2A has been implicated in
343 AMPK dephosphorylation and inactivation in non-neuronal cells[53]. The dynamic oscillatory
344 activation of AMPK would enable fine spatiotemporal tuning of mitochondrial dynamics in
345 response to the local activity states in dendritic compartments. The controlled fission and
346 mitophagy is critical for the maintenance of mitochondrial quality in developing dendrites, as the
347 inhibition of AMPK-dependent mitophagy caused aberrant elongation and dysfunction of
348 mitochondria.

349 Intriguingly, the CaMKK2-AMPK pathway regulating MFF and ULK2 activities has been
350 implicated in the excessive mitochondrial fission and mitophagy in degenerating dendrites in
351 Alzheimer's disease models[26,27]. It is suggested that disruption of Ca^{2+} homeostasis overactivates
352 the CaMKK2-AMPK pathway in these neurons. Thus, Ca^{2+}-sensitive activation of AMPK could
353 be a double-edged sword, promoting dendritic growth by regulating mitochondria turnover during
354 normal development, while contributing to neurodegeneration by excessive mitochondrial
355 degradation under pathological conditions.

356 It has been shown that genetic deletions of AMPK subunits exhibit little or no cell-

357 autonomous defects in neuronal development in mice[54–57]. Conditional deletion of AMPKα1/α2
358 (AMPKα1−/−; AMPKα2F/F; Emx1-Cre) exhibits no overt phenotypes in the polarization and
359 survival of cortical neurons, except for the thinning of the cortical layer at P3[55,58]. In contrast,
360 acute treatment with AICAR or metformin induces rapid AMPK phosphorylation and disrupts
361 axon formation in cultured cortical neurons[59]. Thus, AMPK is thought to be dispensable for
362 neuronal differentiation during normal development, but exerts its effects when overactivated
363 under stress conditions. In the present study, we show that defects in mitochondrial dynamics and
364 dendrite growth by acute AMPK inhibition are evident only in differentiating neurons in the first
365 postnatal week, and that they recovered in later stages in vivo. It is therefore possible that the
366 transient morphological changes might have been overlooked in previous studies. Mild and
367 transient phenotypes by chronic inhibition of AMPK might be due to the robust multi-step
368 regulation of mitochondrial dynamics. In mature neurons, long-term potentiation (LTP) of
369 synaptic activity causes mitochondrial fission via CaMKII and Drp1 phosphorylation[31]. The
370 intracellular Ca^{2+} rise also induces a distinct type of mitochondrial fission initiated from the inner
371 mitochondrial membrane[60]. AMPK might predominantly mediate spontaneous activity before
372 synaptic maturation, while other mechanisms may take over and control mitochondrial fission in
373 more mature neurons. Although no overt histological defects were found in mature neurons of
374 AMPK-deficient mice, whether these neurons form and operate normal neural circuits has not
375 been assessed. Whether AMPK has a distinct function in dendrites of mature neurons is one of
376 many important questions that entail further study.
377 The present study highlights a new role of AMPK in mitochondrial homeostasis in normal
378 development of neurons in addition to its major role in safeguarding neurons from energetic stress.
379 Dynamic activation and inactivation of AMPK by neuronal activity are clearly important for the
380 fine-tuning of mitochondrial homeostasis. Thus, future work should focus on the precise
381 dynamics and mechanism of AMPK activation, as well as inactivation, for a new perspective on
382 the physiology and pathology of AMPK signals.
383
384

385 **Methods**

386

387 **Mice**

388 All animals were treated in accordance with the guidelines of the Animal Experiment Committee
389 of Kyoto University. ICR mice were kept in a 12 hr dark/light cycle at 23 ± 3°C/ 50% humidity,
390 with standard food and water provided ad libitum, in group housing of up to three animals per
391 cage.

392

393 **Reagents**

394 Reagents used in this study were as follows: D, L-APV (APV, 200 μM, Sigma Aldrich, A5282),
395 Tetrodotoxin (TTX, 0.5 μM, Abcam, ab120054), AICAR (1-2 mM, AdipoGen. Inc, AG-CR1-
396 0061), Compound C (CC, Dorsomorphin, 20 μM, Nacalai, 18768-04), L-Glutamic acid
397 (Glutamate, 100 μM, Sigma-Aldrich, G1251), STO-609 (10 μM, MedChem Express, HY-19805),
398 Pim1/AKK1-IN-1 (1 μM, MedChem Express, HY-10371), TMRM (20 nM, Fujifilm, 203-18041),
399 Mito-SOX (500 nM, Invitrogen, M36008).

400

401 **Plasmids**

402 pCAG-EGFP, pAAV-CAG-Mito-DsRed and pAAV-CAG-Mito-EGFP were constructed as
403 previously described[1,61]. For RNAi experiments, the target sequences for scramble control (5'-
404 GACATTTCATCCGTTTAGTTA-3'), AMPKα1 sh#1 (5'-GGCACACCCTGGATGAATTAA-
405 3'), AMPKα1 sh#2 (5'-GTTGTAAACCCCTATTATTTG-3'), AMPKα2 sh#1 (5'-
406 GGTAGACAGTCGGAGCTATCT-3'), AMPKα2 sh#2 (5'-GACAATCGGAGAATAATGAAC-
407 3'), and CaMKK2 (5'-CCCTTTCATGGATGAACGAAT-3') were cloned into pBAsi-hH1 vector
408 (Takara, 3220). pCAG-AMPKα1(WT) and pCAG-AMPKα2 (WT) plasmids were created by
409 PCR amplification of cDNAs for AMPKα1 (NCBI Reference Sequence: NM_001013367.3) and
410 AMPKα2 (NCBI Reference Sequence: NM_178143.2) from a mouse brain cDNA library and
411 inserted into the pCAGGS vector. Resistant mutants of AMPKα1 and AMPKα2 that contained
412 three silent mutations within the respective shRNA target sequences were generated using the
413 Primestar mutagenesis protocol. pPBbsr2-4031NES (AMPKAR-EV) was a gift from Michiyuki
414 Matsuda. pCAG-jRGECO1a plasmid was generated by subcloning the jRGECO1a sequence from
415 pGP-CMV-NES-jRGECO1a (a gift from Masayuki Sakamoto) into the pCAGGS vector. The
416 pX458-CAG-dCas9KRAB-2A-GFP plasmid was generated by subcloning the CAG promoter
417 from pCAGGS and the dCas9KRAB sequence from CRISPR-dCas9KRAB (a gift from Kuniya

418 Abe) into the pX458 vector (Addgene plasmid #48138). For CRISPR interference experiments,
419 the gRNA sequence for AMPKα2 (5'-TGCCGAAGGTGCCGACGCCCAGG-3') was inserted
420 into pX458-CAG-dCas9KRAB-2A-GFP.
421
422 **Cell cultures and transfection**
423 Primary cultures of hippocampal neurons were prepared as previously described with a few
424 modifications[32]. In brief, postnatal day 0 (P0) mouse hippocampi were dissected, dissociated
425 using Neuron Dissociation Solutions (Fujifilm, 291-78001), and plated on poly-D-lysine (Sigma-
426 Aldrich, P6407) coated coverslips at a density of $3.0 \sim 3.5 \times 10^5$ cells/cm^2 in MEM (Gibco,
427 11095080) supplemented with 10% horse serum (Gibco, 26050070), 0.6% D-glucose, 1 mM
428 sodium pyruvate (Sigma-Aldrich, S8636), and 1% penicillin-streptomycin. Three hours after
429 plating, media was replaced with Neurobasal medium (Gibco, 21103049) supplemented with 2%
430 (v/v) B-27 (Gibco, 17504044) and 0.25% (v/v) GlutaMax (Gibco, 35050061). All neurons were
431 maintained at 37°C in 5% CO_2. Five μM AraC (Sigma-Aldrich, C1768) was added at DIV3.
432 Neurons were transfected at DIV3 using Lipofectamine 2000 (Thermo Fisher Scientific,
433 11668019) according to the manufacturer's instructions. The CRISPRi plasmid was transfected
434 at DIV2.
435 HEK293T cells (Riken BRC Cell Bank, RCB2202) were cultured in DMEM (Gibco, 11965-092)
436 supplemented with 10% Fetal Bovine Serum (FBS, Sigma-Aldrich, F7524), 100 units/mL
437 penicillin and 100 ug/mL streptomycin (Gibco, 15140-122) at 37°C in 5% CO_2. Cells were
438 passaged every 2-3 days and maintained in plastic cell culture-treated dishes. shRNA constructs
439 were transfected using Lipofectamine 2000.
440
441 **Western blotting**
442 Cells were harvested in RIPA lysis buffer (50 mM Tris HCl (pH 7.4), 150 mM sodium chloride,
443 0.25% (w/v) Sodium Deoxycholate, 1% (v/v) NonidetP-40, 1 mM EDTA, and Protease and
444 phosphatase inhibitor cocktail (Thermo Fisher Scientific, 78442)). Lysates were subjected to
445 SDS-PAGE and immunoblotting.
446 Primary antibodies used were the following: mouse anti-GFP (1:5000, Thermo Fisher
447 Scientific, A11120); rabbit anti-AMPKα1 (1:3000, Abcam, ab32047); rabbit anti-AMPKα2
448 (1:3000, Abcam, ab3760); rabbit anti-AMPKα (1:1000, Cell Signaling Technology, 2532); rabbit
449 anti-phospho-AMPKα (Thr172) (1:1000, Cell Signaling Technology, 2535); rabbit anti-MFF
450 (1:3000, Proteintech, 17090-1-AP); rabbit anti-phospho-MFF (Ser172/146) (1:1000, Affinity

451 Biosciences, AF2365); rabbit anti-ULK1 (1:2000, Cell Signaling Technology, 8054); rabbit anti-
452 phospho-ULK1 (Ser555) (1:1000, Cell Signaling Technology, 5869); rabbit anti-PGC1α (1:5000,
453 Abcam, ab191838) and HRP-conjugated mouse anti-beta actin (1:10000, Santa Cruz, sc-47778
454 HRP). The secondary antibodies used were the following: HRP-conjugated goat anti-mouse IgG
455 (1:10000, Bio-Rad, 170-6516); HRP-conjugated goat anti-rabbit IgG (1:10000, Bio-Rad, 170-
456 6515).
457
458 **In utero electroporation**
459 Pregnant mice on day 14.5 of gestation were deeply anesthetized via the intra-abdominal injection
460 of a mixture of medetomidine, midazolam and butorphanol. Plasmid DNA diluted with saline
461 containing 0.01% Fast Green was injected into the lateral ventricle of mouse embryos with a glass
462 needle. Four current pulses (amplitude, 40 V; duration, 50 ms; intervals, 950 ms) were delivered
463 with a forceps-shaped electrode (CUY650P3, NepaGene) connected to an electroporator (CUY21,
464 NepaGene). Concentrations of the plasmids used are as follows: pCAG-EGFP (0.2 μg/μl);
465 shRNA-scramble control (3-6 μg/μl); shRNA- AMPKα2 (3-6 μg/μl); CRISPRi gRNA-empty (5
466 μg/μl); and CRISPRi gRNA- AMPKα2 (5 μg/μl).
467
468 **Immunofluorescence and image acquisition**
469 For immunocytochemistry, cultured cells were fixed with 4% PFA in PBS and permeabilized with
470 PBS containing 0.25% Triton X-100 (PBS-T). Cells were then blocked with blocking solution
471 (PBS with 2% BSA) and incubated with rabbit anti-AMPKα2 primary antibody (1:200,
472 Proteintech, 18167-1-AP) at 4°C overnight. After washing with PBS, cells were incubated with
473 goat anti-Rabbit Alexa Fluor 647 (1:400, Invitrogen, A21244) secondary antibody at 4°C
474 overnight.
475 For immunohistochemistry, the mice at P5 or P10 were perfused with PBS followed
476 by 4% paraformaldehyde (PFA) in phosphate buffer. Their brains were removed and postfixed for
477 2-3 hrs at 4°C. After washing with PBS, the brains were embedded in 3.5% low-melting agarose
478 in PBS. The brains were then sectioned into 200 μm thick sagittal slices with a vibratome (NLS-
479 AT, Dosaka EM). The sections were permeabilized in PBS with 0.25 % Triton (PBS-T) for 15
480 min and blocked with 2% skim milk in PBS-T for 30 min. The sections were incubated with a
481 chick anti-GFP (1:2000, Invitrogen, A10262) primary antibody in blocking solution at 4°C
482 overnight, followed by incubation with a goat anti-Chicken Alexa Fluor 488 (1:400, Invitrogen,
483 A11039) secondary antibodies at 4°C overnight.

484 Images of the fixed samples were acquired with a laser scanning confocal microscope
485 (FV1000, Olympus) equipped with UPlanSApo 20× (N.A. 0.75), UPLSAPO 40× (NA 0.95)
486 objectives, or a spinning disk confocal microscope (Dragonfly, Andor) equipped with Nikon
487 PLAN APO 40× (Silicone oil, NA 1.25), Apo TIRF 100× (oil-immersion, NA 1.49) objectives.
488 For morphometric analysis, dendrites were traced using the ImageJ plugin Simple
489 Neurite Tracer (SNT). Total dendrite length and the number of branches were calculated using
490 MATLAB software. For quantification of dendritic mitochondrial densities (ratio of
491 mitochondrial area to dendrite area), acquired images were binarized and the areas filled with
492 Mito-DsRed signals and volume marker GFP signals were quantified using ImageJ.
493 For p62 analysis, hippocampal neurons transfected with GFP and mito-DsRed were
494 fixed at DIV5 and immunostained with guinea pig anti-p62 primary antibody (1:100, Progen,
495 GP62-C,) and goat anti-Guinea Pig Alexa Fluor 633 secondary antibody (1:400, Invitrogen,
496 A21105). The number of p62 puncta in dendrites was counted using the ImageJ plugin Find
497 Maxima. For colocalization analysis of p62 puncta and mitochondria, Mander's overlap
498 coefficient was calculated from anti-p62 signals and mito-DsRed signals in dendrites using the
499 ImageJ plugin JaCoP. Surface rendering was done with Imaris software.
500
501 **Time-lapse imaging and image analysis**
502 For time-lapse imaging of mitochondrial dynamics, cultured hippocampal neurons were
503 transfected on DIV3 with pCAG-EGFP and pAAV-CAG-mitoDsRed plasmids. Time-lapse
504 images were acquired every 3 s for 20 min at DIV5 using a spinning-disc confocal microscope
505 (CV1000, Yokogawa) with a UPLSApo 100× objective (Oil immersion, N.A. 1.4, Olympus) at
506 37°C with 5% CO_2 flow. The mitochondrial movement was tracked using the ImageJ plugin
507 MTrackJ. The mitochondrial fission and fusion events were counted manually. Peripheral and
508 midzone mitochondrial fissions were defined as events in which the relative position of the
509 fission site along the length axis was 0~25% and 25~50%, respectively. The percentage of
510 motile mitochondria was calculated by dividing the number of mitochondria that were displaced
511 more than 4 μm from their original positions within 20 minutes by the total number of
512 mitochondria. A continuous movement of mitochondria (> 1.5 μm for > 6 sec) was defined as
513 one moving event, and their speed was calculated by using MATLAB software.
514 For AMPK FRET imaging, cultured hippocampal neurons transfected with AMPKAR-
515 EV were imaged every 3 sec for 3min at DIV5 with an inverted epifluorescence microscope
516 (IX83, Olympus) equipped with LUCPlanFLN 20× (NA 0.45), UplanSApo 40× (Silicone oil,

517 NA 1.25) objectives. For dual imaging of AMPK FRET and calcium imaging, cultured
518 hippocampal neurons were cotransfected with AMPKAR-EV and jRGECO1a, and imaged
519 every 5 sec for 5 min. Fluorescence images were acquired with the following filters and mirrors:
520 excitation filters FF02-438/24-25 (for CFP/ YFP); a dichroic mirror FF458-Di02-25x36 (for
521 CFP/ YFP); emission filters FF01-483/32-25 (for CFP); FF01-542/27-25 (for YFP); and filter
522 sets U-FMCHE (Ex 565-585 nm/ DM 595/ Em 600-690) (for jRGECO1a).
523 For FRET ratio analysis, after background subtraction, the YFP/CFP fluorescence
524 intensity ratio was calculated in the ROI of the proximal dendritic region. The YFP/CFP ratio
525 was plotted along the time axis, and the FRET peak frequency was quantified using the
526 MATLAB findpeaks function with a threshold for peak heights greater than 0.05. The Cross-
527 Correlation Function was calculated followed methods described previously [62] using MATLAB
528 software.
529 For TMRM imaging, cultured hippocampal neurons transfected with mito-EGFP
530 were incubated with 20 nM TMRM 1-2 h prior to imaging. Time-lapse images were acquired
531 every 5 sec for 10 min at DIV5 with a spinning-disc confocal microscope (CV1000, Yokogawa)
532 equipped with a UPLSApo 100× objective (Oil immersion, N.A. 1.4, Olympus).
533 For TMRM intensity analysis, after background subtraction, TMRM intensity in
534 individual mitochondria was divided by the mitochondrial area. TMRM flickering, defined as a
535 transient loss of TMRM intensity to the background level, was scored as the number of
536 flickering events that occurred within 10 minutes in the soma and proximal dendrites, divided
537 by the mitochondrial area.
538 For quantification of mitochondrial ROS, cultured hippocampal neurons transfected
539 with mito-EGFP at DIV3 were incubated with 500 nM Mito-SOX for 15 min at DIV5 and then
540 the Mito-Sox was washed out. Time-lapse imaging was initiated 18-20 h after treatment, using a
541 spinning-disc confocal microscope (CV1000, Yokogawa) equipped with a UPLSApo 100×
542 objective (Oil immersion, N.A. 1.4, Olympus). Mito-SOX intensity in individual mitochondria
543 (($F_{mitochondria}$/ $F_{background}$)/ (Mitochondrial Area)) was quantified using ImageJ.
544

Acknowledgements

We thank Dr. Michiyuki Matsuda for the AMPKAR-EV plasmid, Dr. Yoshiaki Tagawa for the GCaMP6s plasmid, Dr. Masayuki Sakamoto for the jRGECO1a plasmid, Drs. Kuniya Abe, Yusuke Kishi, Shinnosuke Suzuki, Ryuta Kinoshita for the CRISPR-dCas9KRAB plasmid, iCeMS Analysis Center for technical assistance with microscopy, Drs. Takaki Miyata, Mayumi Okamoto, Daniel Packwood for advice, Dr. James Hejna for critical reading of the manuscript.

Author contributions

Conceptualization: A.H., K.F., M.K.; Methodology: A.H., K.F., A.K., N.O., M.K.; Investigation: A.H., J.K., K.F.; Writing - original draft: M.K. and A.H., and all the authors read and commented on the manuscript.

Funding

This work was supported by the Japan Society for the Promotion of Science (JSPS) Kakenhi (20H00483 and JP16H06280) and the Uehara Memorial Foundation to M.K., and a JST spring grant (JPMJSP2110) to A.H.

562 **Reference**

563 1. Fukumitsu, K. *et al.* Synergistic Action of Dendritic Mitochondria and Creatine Kinase
564 Maintains ATP Homeostasis and Actin Dynamics in Growing Neuronal Dendrites. *J.*
565 *Neurosci.* **35**, 5707–5723 (2015).
566 2. Sheng, Z. H. & Cai, Q. Mitochondrial transport in neurons: Impact on synaptic
567 homeostasis and neurodegeneration. *Nat. Rev. Neurosci.* **13**, 77–93 (2012).
568 3. Rangaraju, V. *et al.* Pleiotropic Mitochondria: The Influence of Mitochondria on
569 Neuronal Development and Disease. *J. Neurosci.* **39**, 8200–8208 (2019).
570 4. Schon, E. A. & Przedborski, S. Mitochondria: The Next (Neurode) Generation. *Neuron*
571 **70**, 1033–1053 (2011).
572 5. Pekkurnaz Gulcin & Wang, X. Mitochondrial heterogeneity and homeostasis through the
573 lens of a neuron. *Nat. Metab.* (2022). doi:10.1038/s42255-022-00594-w
574 6. Youle, R. J. *et al.* Mitochondrial Fission, Fusion, and Stress. *Science* **337**, 1062–1065
575 (2012).
576 7. Gandre-Babbe, S. & van der Bliek, A. M. The Novel Tail-anchored Membrane Protein
577 Mff Controls Mitochondrial and Peroxisomal Fission in Mammalian Cells. *Mol. Biol.*
578 *Cell* **19**, 2402–2412 (2008).
579 8. Palmer, C. S. *et al.* MiD49 and MiD51, new components of the mitochondrial fission
580 machinery. *EMBO Rep.* **12**, 565–573 (2011).
581 9. Yoon, Y., Krueger, E. W., Oswald, B. J. & McNiven, M. A. The Mitochondrial Protein
582 hFis1 Regulates Mitochondrial Fission in Mammalian Cells through an Interaction with
583 the Dynamin-Like Protein DLP1. *Mol. Cell. Biol.* **23**, 5409–5420 (2003).
584 10. Li, Z., Okamoto, K. I., Hayashi, Y. & Sheng, M. The importance of dendritic
585 mitochondria in the morphogenesis and plasticity of spines and synapses. *Cell* **119**, 873–
586 887 (2004).
587 11. Ishihara, N. *et al.* Mitochondrial fission factor Drp1 is essential for embryonic
588 development and synapse formation in mice. *Nat. Cell Biol.* **11**, 958–966 (2009).
589 12. Fukumitsu, K. *et al.* Mitochondrial fission protein Drp1 regulates mitochondrial
590 transport and dendritic arborization in cerebellar Purkinje cells. *Mol. Cell. Neurosci.* **71**,
591 56–65 (2016).
592 13. Chen, H., Mccaffery, J. M. & Chan, D. C. Mitochondrial Fusion Protects against
593 Neurodegeneration in the Cerebellum. *Cell* **130**, 548–562 (2007).
594 14. Wang, X. *et al.* Impaired balance of mitochondrial fission and fusion in Alzheimer's

595 disease. *J. Neurosci.* **29**, 9090–9103 (2009).
596 15. Herzig, S. & Shaw, R. J. AMPK: Guardian of metabolism and mitochondrial
597 homeostasis. *Nat. Rev. Mol. Cell Biol.* **19**, 121–135 (2018).
598 16. Ducommun, S. *et al.* Motif affinity and mass spectrometry proteomic approach for the
599 discovery of cellular AMPK targets : Identi fication of mitochondrial fission factor as a
600 new AMPK substrate. *Cell. Signal.* **27**, 978–988 (2015).
601 17. Toyama, E. Q. *et al.* AMP-activated protein kinase mediates mitochondrial fission in
602 response to energy stress. *Science.* **351**, 275–281 (2016).
603 18. Jäer, S., Handschin, C., St-Pierre, J. & Spiegelman, B. M. AMP-activated protein kinase
604 (AMPK) action in skeletal muscle via direct phosphorylation of PGC-1α. *Proc. Natl.*
605 *Acad. Sci. U. S. A.* **104**, 12017–12022 (2007).
606 19. Chen, Z. *et al.* Global phosphoproteomic analysis reveals ARMC10 as an AMPK
607 substrate that regulates mitochondrial dynamics. *Nat. Commun.* **10**, (2019).
608 20. Egan, D. F. *et al.* Phosphorylation of ULK1 (hATG1) by AMP-Activated Protein Kinase
609 Connects Energy Sensing to Mitophagy. *Science.* **331**, 456–461 (2011).
610 21. Kim, J., Kundu, M., Viollet, B. & Guan, K. L. AMPK and mTOR regulate autophagy
611 through direct phosphorylation of Ulk1. *Nat. Cell Biol.* **13**, 132–141 (2011).
612 22. Tilokani, L. *et al.* AMPK-dependent phosphorylation of MTFR1L regulates
613 mitochondrial morphology. *Sci. Adv.* **8**, 1–20 (2022).
614 23. Hawley, S. A. *et al.* Complexes between the LKB1 tumor suppressor, STRADα/β and
615 MO25α/β are upstream kinases in the AMP-activated protein kinase cascade. *J. Biol.* **2**,
616 1–16 (2003).
617 24. Hawley, S. A. *et al.* Calmodulin-dependent protein kinase kinase-β is an alternative
618 upstream kinase for AMP-activated protein kinase. *Cell Metab.* **2**, 9–19 (2005).
619 25. Hurley, R. L. *et al.* The Ca2+/calmodulin-dependent protein kinase kinases are AMP-
620 activated protein kinase kinases. *J. Biol. Chem.* **280**, 29060–29066 (2005).
621 26. Mairet-Coello, G. *et al.* The CAMKK2-AMPK Kinase Pathway Mediates the
622 Synaptotoxic Effects of Aβ Oligomers through Tau Phosphorylation. *Neuron* **78**, 94–108
623 (2013).
624 27. Lee, A. *et al.* Aβ42 oligomers trigger synaptic loss through CAMKK2-AMPK-
625 dependent effectors coordinating mitochondrial fission and mitophagy. *Nat. Commun.*
626 **13**, 1–20 (2022).
627 28. Redmond, L., Kashani, A. H. & Ghosh, A. Calcium regulation of dendritic growth via

628 CaM kinase IV and CREB-mediated transcription. *Neuron* **34**, 999–1010 (2002).
629 29. Wong, R. O. L. & Ghosh, A. Activity-dependent regulation of dendritic growth and
630 patterning. *Nat. Rev. Neurosci.* **3**, 803–812 (2002).
631 30. Konur, S. & Ghosh, A. Calcium signaling and the control of dendritic development.
632 *Neuron* **46**, 401–405 (2005).
633 31. Divakaruni, S. S. *et al.* Long-Term Potentiation Requires a Rapid Burst of Dendritic
634 Mitochondrial Fission during Induction. *Neuron* **100**, 860-875.e7 (2018).
635 32. Wu, Y. K., Fujishima, K. & Kengaku, M. Differentiation of apical and basal dendrites in
636 pyramidal cells and granule cells in dissociated hippocampal cultures. *PLoS One* **10**, 1–
637 16 (2015).
638 33. Spronsen, M. V. *et al.* TRAK/Milton Motor-Adaptor Proteins Steer Mitochondrial
639 Trafficking to Axons and Dendrites. *Neuron* **77**, 485–502 (2013).
640 34. Faits, M. C., Zhang, C., Soto, F. & Kerschensteiner, D. Dendritic mitochondria reach
641 stable positions during circuit development. *Elife* **5**, 1–17 (2016).
642 35. Loss, O. & Stephenson, F. A. Developmental changes in trak-mediated mitochondrial
643 transport in neurons. *Mol. Cell. Neurosci.* **80**, 134–147 (2017).
644 36. Lewis, T. L., Kwon, S. K., Lee, A., Shaw, R. & Polleux, F. MFF-dependent
645 mitochondrial fission regulates presynaptic release and axon branching by limiting
646 axonal mitochondria size. *Nat. Commun.* **9**, 1–15 (2018).
647 37. Konagaya, Y. *et al.* A Highly Sensitive FRET Biosensor for AMPK Exhibits
648 Heterogeneous AMPK Responses among Cells and Organs. *Cell Rep.* **21**, 2628–2638
649 (2017).
650 38. Sample, V., Ramamurthy, S., Gorshkov, K., Ronnett, G. V. & Zhang, J. Polarized
651 activities of AMPK and BRSK in primary hippocampal neurons. *Mol. Biol. Cell* **26**,
652 1935–1946 (2015).
653 39. Barnes, A. P. *et al.* LKB1 and SAD Kinases Define a Pathway Required for the
654 Polarization of Cortical Neurons. *Cell* **129**, 549–563 (2007).
655 40. Courchet, J. *et al.* Terminal Axon Branching Is Regulated by the LKB1-NUAK1 Kinase
656 Pathway via Presynaptic Mitochondrial Capture. *Cell* **153**, 1510–1525 (2013).
657 41. Weisová, P., Concannon, C. G., Devocelle, M., Prehn, J. H. M. & Ward, M. W.
658 Regulation of glucose transporter 3 surface expression by the AMP-activated protein
659 kinase mediates tolerance to glutamate excitation in neurons. *J. Neurosci.* **29**, 2997–3008
660 (2009).

661 42. Connolly, N. M. C., Düssmann, H., Anilkumar, U., Huber, H. J. & Prehn, J. H. M.
662 Single-cell imaging of bioenergetic responses to neuronal excitotoxicity and oxygen and
663 glucose deprivation. *J. Neurosci.* **34**, 10192–10205 (2014).
664 43. Wayman, G. A. *et al.* Regulation of Axonal Extension and Growth Cone Motility by
665 Calmodulin-Dependent Protein Kinase I. *J. Neurosci.* **24**, 3786–3794 (2004).
666 44. Wayman, G. A. *et al.* Activity-Dependent Dendritic Arborization Mediated by CaM-
667 Kinase I Activation and Enhanced CREB-Dependent Transcription of Wnt-2. *Neuron*
668 **50**, 897–909 (2006).
669 45. Kleele, T. *et al.* Distinct fission signatures predict mitochondrial degradation or
670 biogenesis. *Nature* **593**, 435–439 (2021).
671 46. Buckman, J. F. & Reynolds, I. J. Spontaneous Changes in Mitochondrial Membrane
672 Potential in Cultured Neurons. *J. Neurosci.* **21**, 5054–5065 (2001).
673 47. Bonora, M., Giorgi, C. & Pinton, P. Molecular mechanisms and consequences of
674 mitochondrial permeability transition. *Nat. Rev. Mol. Cell Biol.* **23**, 266–285 (2022).
675 48. Zorov, D. B., Juhaszova, M. & Sollott, S. J. Mitochondrial reactive oxygen species
676 (ROS) and ROS-induced ROS release. *Physiol. Rev.* **94**, 909–950 (2014).
677 49. Twig, G. *et al.* Fission and selective fusion govern mitochondrial segregation and
678 elimination by autophagy. *EMBO J.* **27**, 433–446 (2008).
679 50. Lewis, S. C., Uchiyama, L. F. & Nunnari, J. ER-mitochondria contacts couple mtDNA
680 synthesis with Mitochondrial division in human cells. *Science.* **353**, (2016).
681 51. DuBoff, B., Götz, J. & Feany, M. B. Tau Promotes Neurodegeneration via DRP1
682 Mislocalization In Vivo. *Neuron* **75**, 618–632 (2012).
683 52. Di Meo, D., Ravindran, P., Sadhanasatish, T., Dhumale, P. & Püschel, A. W. The
684 balance of mitochondrial fission and fusion in cortical axons depends on the kinases
685 SadA and SadB. *Cell Rep.* **37**, 110141 (2021).
686 53. Joseph, B. K. *et al.* Inhibition of AMP kinase by the protein phosphatase 2A
687 heterotrimer, PP2APpp2r2d. *J. Biol. Chem.* **290**, 10588–10598 (2015).
688 54. Dzamko, N. *et al.* AMPK β1 deletion reduces appetite, preventing obesity and hepatic
689 insulin resistance. *J. Biol. Chem.* **285**, 115–122 (2010).
690 55. Williams, T., Courchet, J., Viollet, B., Brenman, J. E. & Polleux, F. AMP-activated
691 protein kinase (AMPK) activity is not required for neuronal development but regulates
692 axogenesis during metabolic stress. *Proc. Natl. Acad. Sci.* **108**, 5849–5854 (2011).
693 56. Ramamurthy, S., Chang, E., Cao, Y., Zhu, J. & Ronnett, G. V. AMPK activation

694 regulates neuronal structure in developing hippocampal neurons. *Neuroscience* **259**, 13–
695 24 (2014).
696 57. Muraleedharan, R. *et al.* AMPK-Regulated Astrocytic Lactate Shuttle Plays a Non-Cell-
697 Autonomous Role in Neuronal Survival. *Cell Rep.* **32**, (2020).
698 58. Muraleedharan, R. & Dasgupta, B. AMPK in the brain: its roles in glucose and neural
699 metabolism. *FEBS J.* 1–16 (2021). doi:10.1111/febs.16151
700 59. Amato, S. *et al.* AMP-activated protein kinase regulates neuronal polarization by
701 interfering with PI3-kinase localization. *Science.* **332**, 247–251 (2011).
702 60. Cho, B. *et al.* Constriction of the mitochondrial inner compartment is a priming event for
703 mitochondrial division. *Nat. Commun.* **8**, 15754 (2017).
704 61. Umeshima, H., Hirano, T. & Kengaku, M. Microtubule-based nuclear movement occurs
705 independently of centrosome positioning in migrating neurons. *Proc. Natl. Acad. Sci. U.*
706 *S. A.* **104**, 16182–7 (2007).
707 62. Kunida, K., Matsuda, M. & Aoki, K. FRET imaging and statistical signal processing
708 reveal positive and negative feedback loops regulating the morphology of randomly
709 migrating HT-1080 cells. *J. Cell Sci.* **125**, 2381–2392 (2012).
710

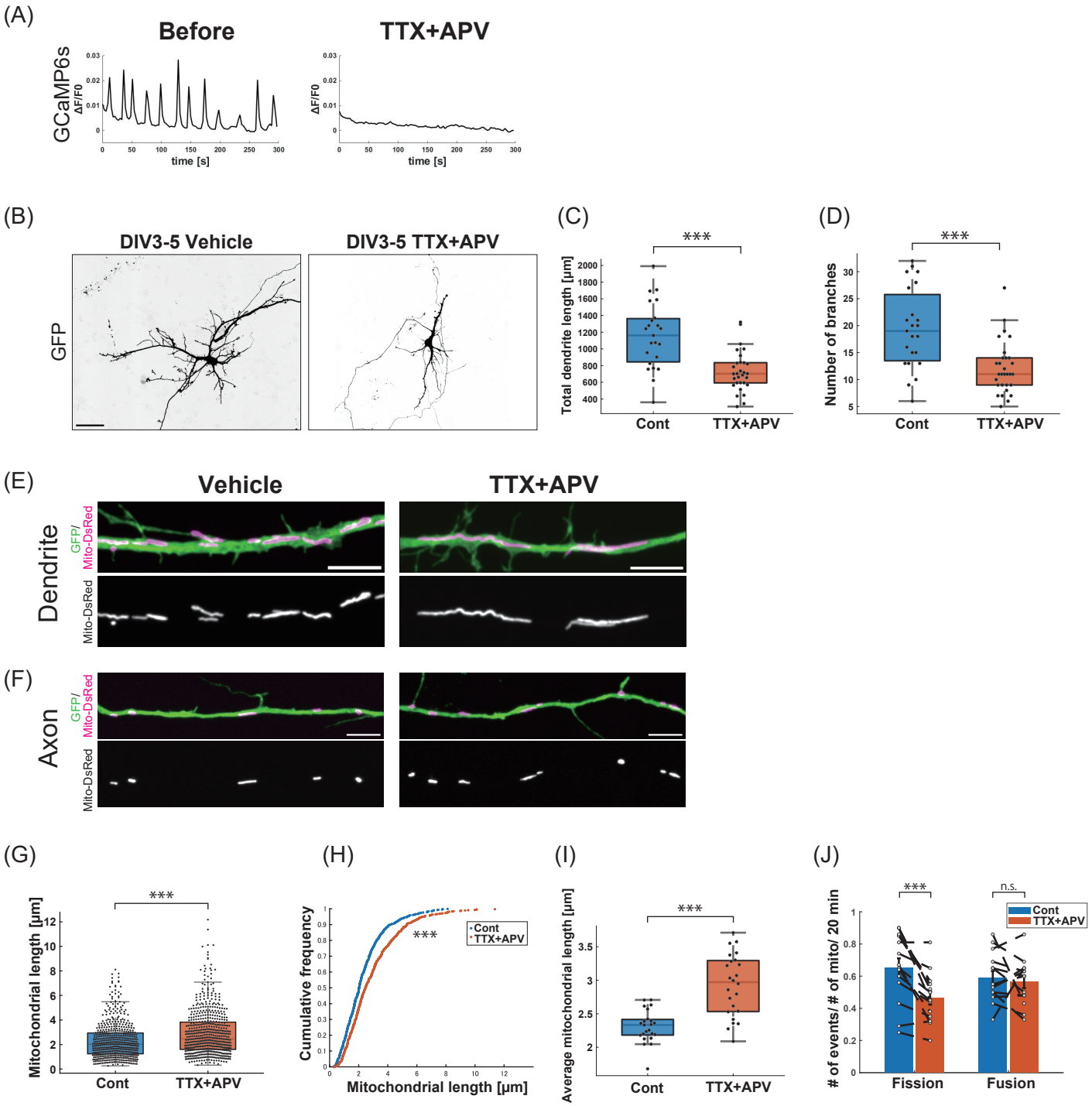

Figure 1. Neuronal activity enhances dendrite formation and mitochondrial fission in developing hippocampal neurons. **(A)** GCAMP6s ΔF/F transients in cultured hippocampal neurons before and after TTX+APV treatment (see also Supplementary Video 1). **(B)** Morphology of hippocampal neurons treated with vehicle or TTX+APV from DIV3 to 5. Cells were labeled with GFP (see also Supplementary Video 2). **(C, D)** Quantification of total dendritic length (C) and number of branch points (D). N= 23 for control cells, 30 for TTX+APV treated cells. ***p= 4.8×10^{-5} (C); ***p= 1.8×10^{-4} (D); Wilcoxon rank-sum test. **(E, F)** Morphology of mitochondria in dendrites (E) and axons (F) of DIV5 hippocampal neurons treated with vehicle or TTX+APV for 6h. Cells were labeled with mito-DsRed and GFP. **(G, H)** Distribution (G) and cumulative frequency (H) of the mitochondrial length in dendrites. N= 576 mitochondria from 23 control cells, 613 mitochondria from 24 drug-treated cells. ***p= 1.3×10^{-9}, Wilcoxon rank-sum test. **(I)** Average length of dendritic mitochondria in individual neurons. N= 23 control cells, 24 TTX+APV treated cells. ***p= 1.2×10^{-5}, Wilcoxon rank-sum test. **(J)** Quantification of the mitochondrial fission and fusion frequencies in dendrites before and 1-3h after TTX+APV treatment. N= 14 cells, mean± SEM, ***p= 4.1×10^{-4} for fission, (n.s.) p= 0.57 for fusion, paired two-tailed t test. Box plots denote the median (50th percentile) and the 25th to 75th percentiles of datasets in (C, D, G, I). Samples were collected from three independent experiments. Scale bars: 50 µm in (B), 5 µm in (E, F).

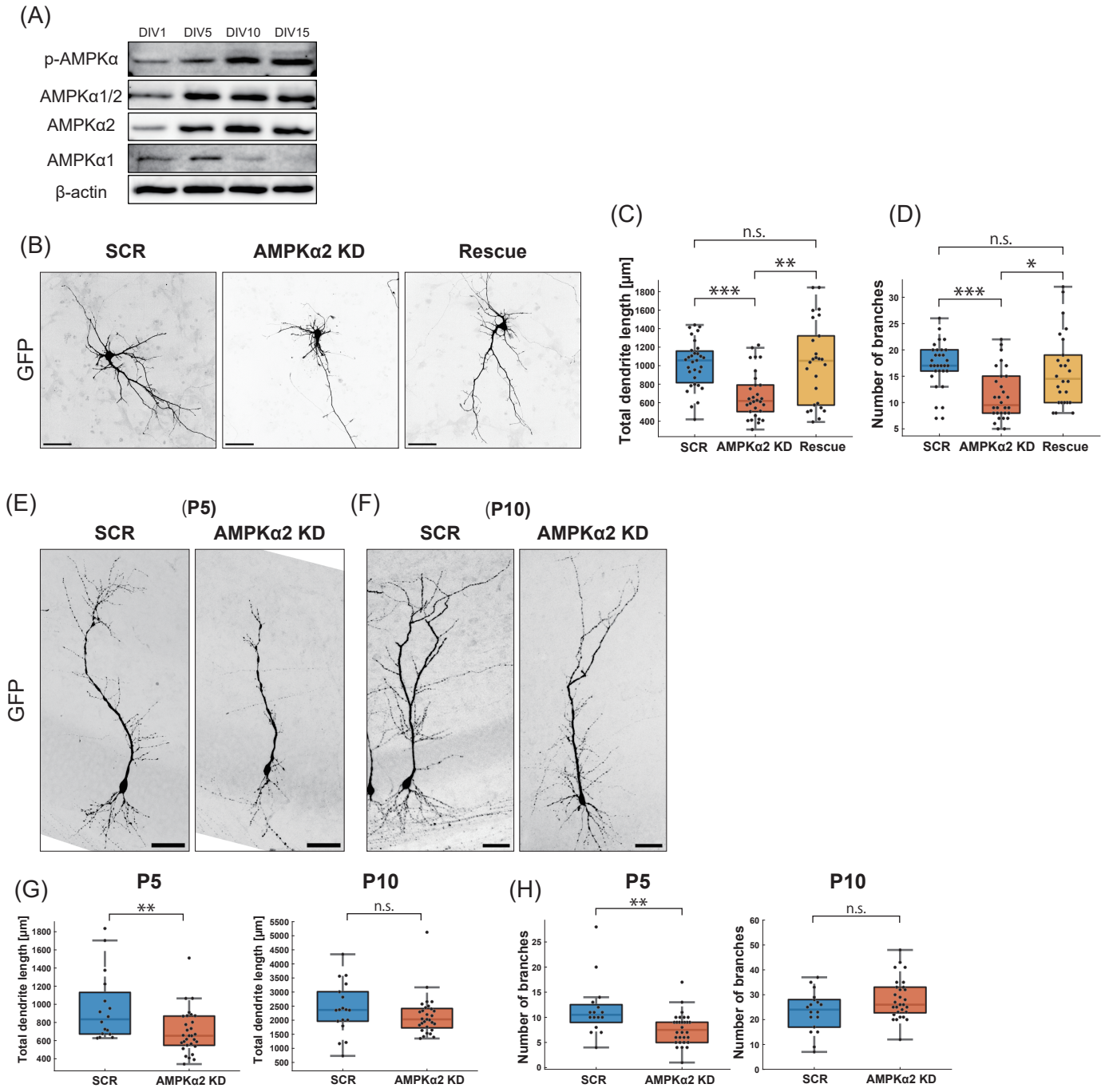

Figure 2. AMPK promotes dendrite formation of hippocampal neurons.

(A) Expression profiles of AMPKα subunits in developing hippocampal neurons in culture. Whole cell lysates were collected at indicated stages and subjected to western blotting with antibodies against AMPKα1 and/or α2, and AMPKα1/2 phosphorylated at threonine 172 (p-AMPKα). **(B)** Morphology of hippocampal neurons transfected with GFP and the following constructs: shRNA-scramble control (SCR); shRNA-AMPKα2 #1 (AMPKα2 KD); or shRNA-AMPKα2 #1 with shRNA-resistant AMPKα2 (Rescue). Cells were transfected at DIV3 and fixed at DIV5. **(C, D)** Quantification of total dendritic length (C) and number of branch points (D). N= 31 cells for SCR, 30 cells for AMPKα2 KD, and 26 cells for Rescue. ***p= 4.0×10^{-4} for SCR vs. AMPKα2 KD, **p= 0.0058 for AMPKα2 KD vs. Rescue (C); ***p= 2.0×10^{-4} for SCR vs. AMPKα2 KD, *p= 0.018 for AMPKα2 KD vs. Rescue (D), Kruskal–Wallis test with Bonferroni multiple comparisons test. **(E, F)** Morphology of CA1 pyramidal neurons transfected with GFP and shRNA-scramble control (SCR) or shRNA-AMPKα2 #1 (AMPKα2 KD) by in utero electroporation at E14.5, followed by fixation at P5 (E) and P10 (F). **(G, H)** Quantification of total dendritic length (G) and number of branch points (H) in CA1 pyramidal neurons at P5 and P10. N≥ 16 cells for SCR and AMPKα2 KD, **p= 0.0067 for P5; (n.s.) p= 0.20 for P10 (G); **p= 0.0021 for P5; (n.s.) p= 0.12 for P10 (H), Wilcoxon rank-sum test. Box plots denote the median (50th percentile) and the 25th to 75th percentiles of datasets in (C, D, G, H). Samples were collected from three independent experiments. Scale bars: 50 μm in (B, E, F).

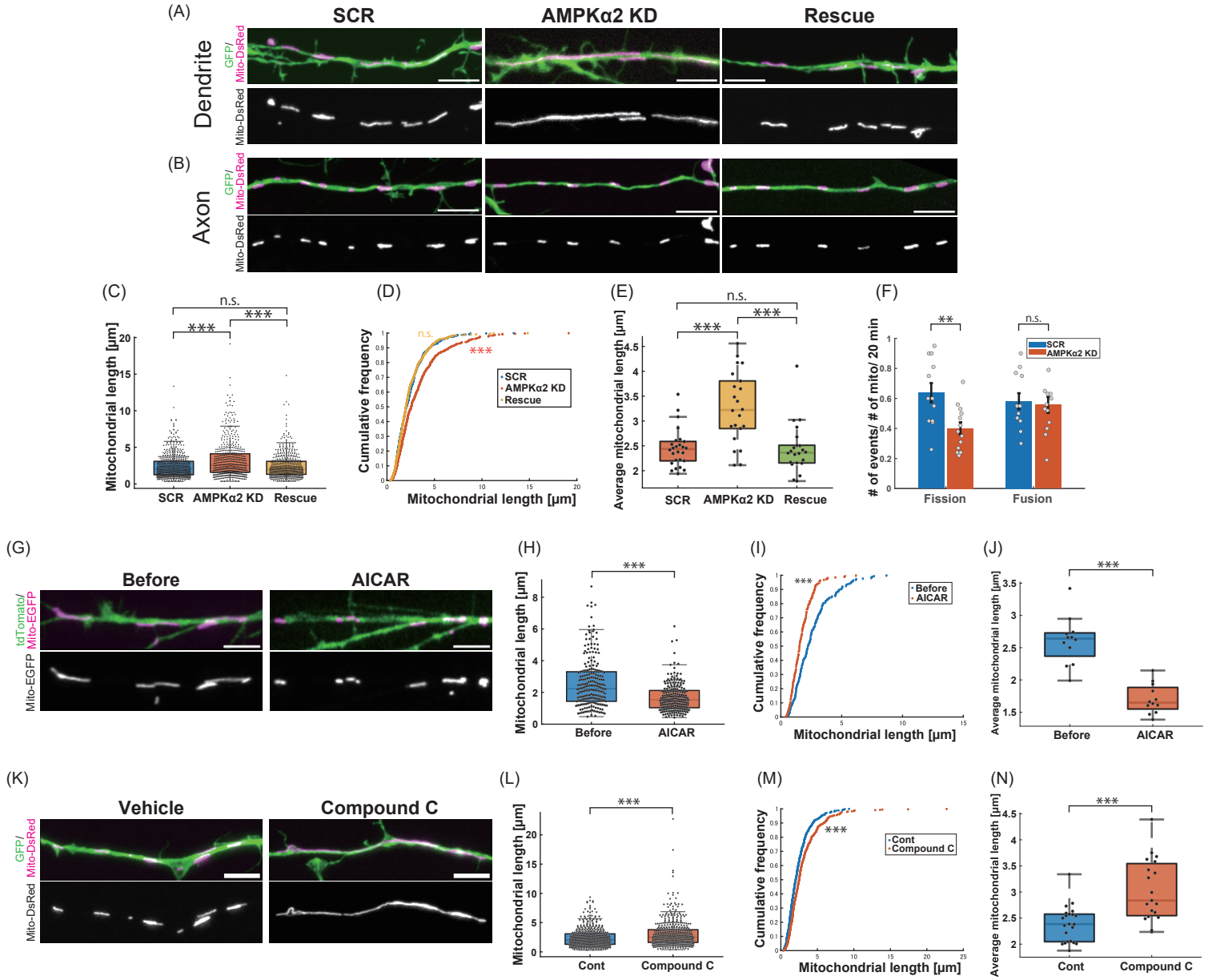

Figure 3. AMPK enhances mitochondrial fission in dendrites of developing hippocampal neurons.

(A, B) Morphology of mitochondria in dendrites (A) and axons (B) in hippocampal neurons transfected with GFP and mito-DsRed together with shRNA-scramble control (SCR), shRNA-AMPKα2#1 (AMPKα2 KD), or shRNA-AMPKα2#1 with shRNA-resistant AMPKα2 (Rescue). Cells were transfected at DIV3 and fixed at DIV5. **(C, D)** Distribution (C) and cumulative frequency (D) of the length of dendritic mitochondria in SCR, AMPKα2 KD and Rescue cells. N= 669 mitochondria from 26 cells (SCR), 548 mitochondria from 22 cells (AMPKα2 KD), and 543 mitochondria from 22 cells (Rescue), respectively. ***p< 0.001; (n.s.) p> 0.05; Kruskal–Wallis test with Bonferroni multiple comparisons test. **(E)** Average length of dendritic mitochondria in individual cells. N=26 cells (SCR), 22 cells (AMPKα2 KD), and 22 cells (Rescue), respectively. ***p< 0.001; (n.s.) p> 0.05; Kruskal–Wallis test with Bonferroni multiple comparisons test. **(F)** Quantification of the mitochondrial fission and fusion frequencies in dendrites in SCR and AMPKα2 KD cells. N= 12 cells for SCR, and 13 cells for AMPKα2 KD. Mean ± SEM, **p= 0.0042; (n.s.) p= 0.75; unpaired two-tailed t test. **(G)** Morphology of dendritic mitochondria in hippocampal neurons before and 3-5 h after treatment with 1 mM AICAR (AMPK activator). Cells were labeled with tdTomato and mito-EGFP. **(H, I)** Distribution (H) and cumulative frequency (I) of the length of dendritic mitochondria before and after AICAR treatment. N= 230 mitochondria from 12 control cells, 228 mitochondria from 12 drug-treated cells, ***p= 1.9×10^{-11}; Wilcoxon rank-sum test. **(J)** Average length of dendritic mitochondria in individual cells. N= 12 cells, *** p= 4.9×10^{-4}, Wilcoxon signed-rank test. **(K)** Morphology of dendritic mitochondria in hippocampal neurons treated with vehicle or 20 μM Compound C for 6h. Cells were labeled with GFP and mito-DsRed. **(L, M)** Distribution (L) and cumulative frequency (M) of the length of dendritic mitochondria treated with vehicle or Compound C. N= 575 mitochondria from 22 control cells, 483 mitochondria from 19 drug-treated cells, ***p= 8.5×10^{-8}, Wilcoxon rank-sum test. **(N)** Average length of the dendritic mitochondria in individual cells. N=22 control cells, 19 drug-treated cells, *** p= 2.9×10^{-4}, Wilcoxon rank-sum test. Box plots denote the median (50th percentile) and the 25th to 75th percentiles of datasets in (C, E, H, J, L, N). Samples were collected from three independent experiments. Scale bars: 5 μm in (A, B, G, K).

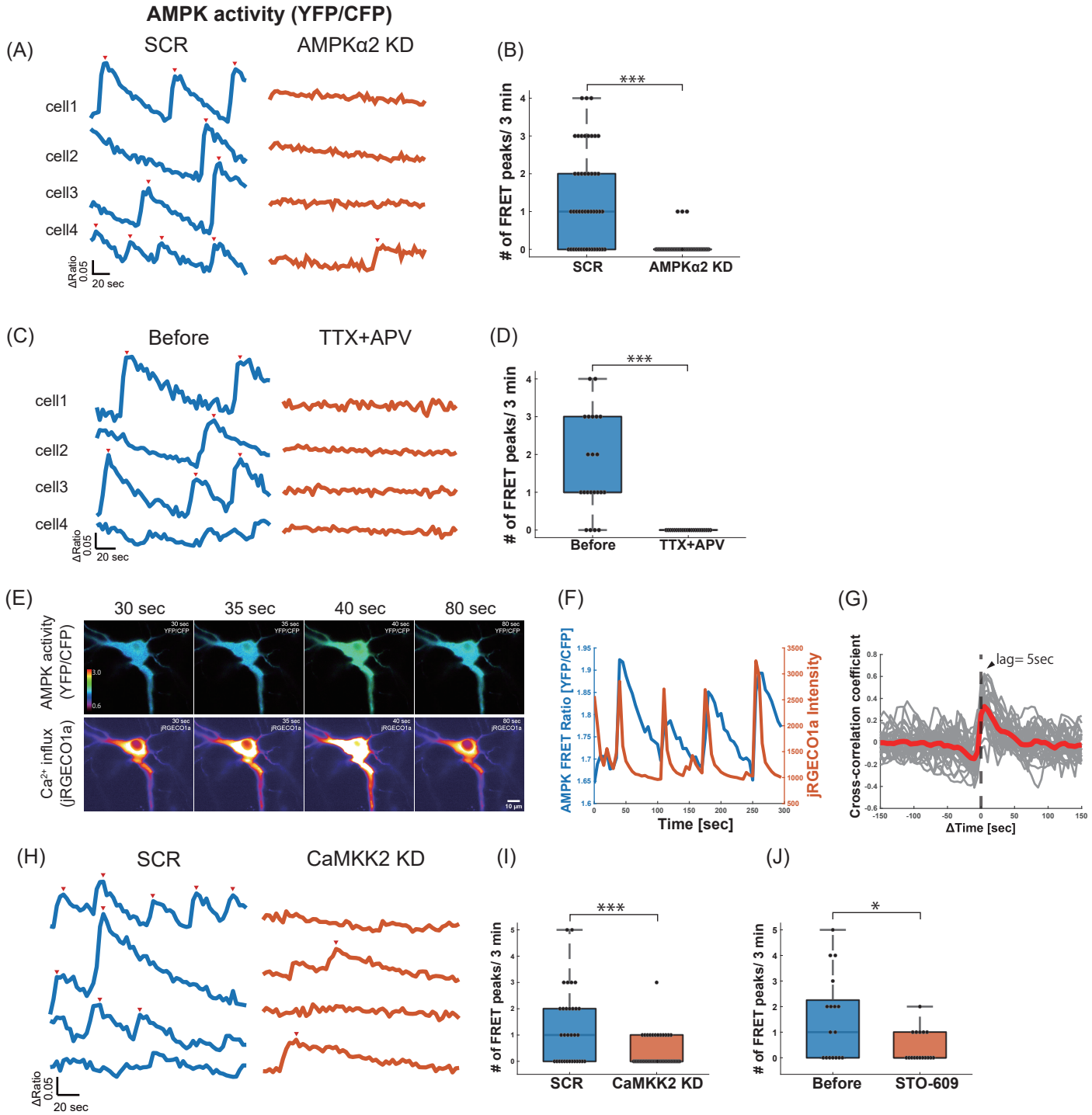

Figure 4. Neuronal activity induces dynamic oscillation of AMPK activity via Ca2+/CaMKK2.

(A) Representative traces of AMPK activity (YFP/CFP ratio) in dendrites of hippocampal neurons expressing AMPKAR-EV with shRNA-scramble control (SCR) or shRNA-AMPKα2 #1 (AMPKα2 KD). Time-lapse images were acquired every 3 sec for 3 min at DIV5 using epifluorescence microscopy. Red arrowheads indicate peaks of AMPK activity. **(B)** Quantification of the frequency of AMPKAR-EV FRET peaks in hippocampal neurons described in (A). N= 46 cells for SCR, 40 cells for AMPKα2 KD; ***p= 1.2×10^{-8}; Wilcoxon rank-sum test. **(C)** Representative traces of AMPK activity in hippocampal neurons expressing AMPKAR-EV before and after TTX+APV treatment. **(D)** Quantification of the frequency of AMPKAR-EV FRET peaks described in (C). N= 22 cells; ***p= 1.6×10^{-4}; Wilcoxon signed-rank test. **(E, F)** Representative time-lapse images and traces of AMPKAR-EV FRET signals and Ca^{2+} influx in hippocampal neurons transfected with AMPKAR-EV and jRGECO1a. Scale bar: 10 μm (E). Blue and orange lines indicate AMPKAR-EV FRET and jRGECO1a signal intensity, respectively (F) (see also Supplementary Video 4). **(G)** The temporal cross-correlations between AMPK activity and Ca^{2+} influx. Gray lines show individual cells, and the red line indicates the average temporal cross-correlation function. The arrowhead shows the highest correlation at 5 sec after Ca^{2+} influx. N= 33 cells. **(H)** Representative traces of AMPK activity in hippocampal neurons expressing AMPKAR-EV with shRNA-scramble control (SCR) or shRNA-CaMKK2 (CaMKK2 KD). **(I)** Quantification of the frequency of AMPKAR-EV FRET peaks described in (H). N=32 cells for SCR, 45 cells for CaMKK2 KD; ***p= 6.8×10^{-4}; Wilcoxon rank-sum test. **(J)** Quantification of the frequency of AMPKAR-EV FRET peaks in hippocampal neurons expressing AMPKAR-EV before and 2h after treatment with 10 μM STO-609 (CaMKK2 inhibitor). N= 17 cells from two independent experiments; *p= 0.011; Wilcoxon signed-rank test. Box plots denote the median (50th percentile) and the 25th to 75th percentiles of datasets in (B, D, I, J). Samples were taken from three independent experiments in (B, D, G, I).

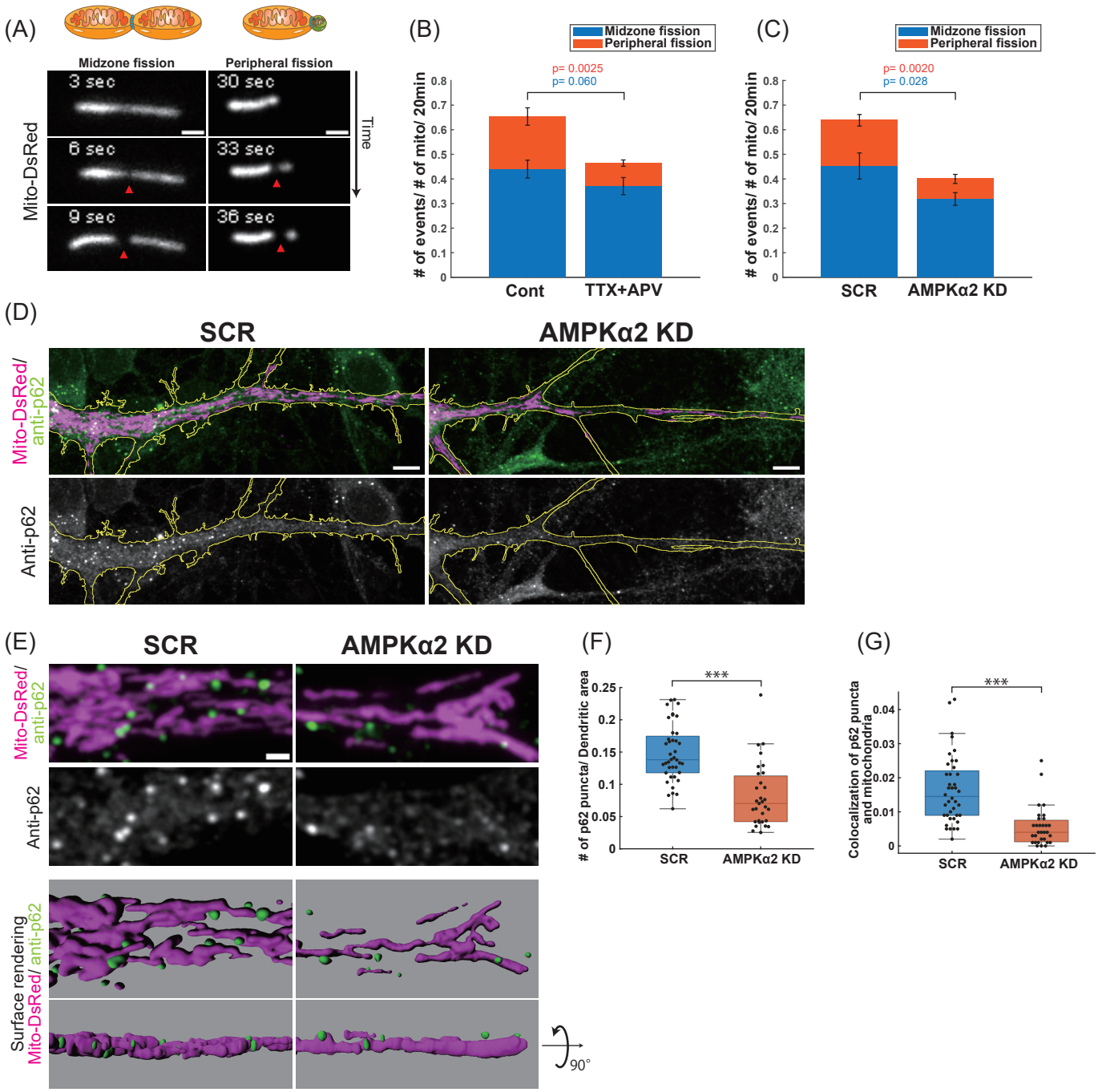

Figure 5. AMPK knockdown suppresses asymmetric mitochondrial fission and mitophagy in growing dendrites. **(A)** Time-lapse images of mitochondria undergoing midzone or peripheral fission in dendrites of hippocampal neurons. Cells were labelled with GFP and mito-DsRed. The red arrows indicate fission sites. **(B)** Quantification of the frequencies of midzone and peripheral fissions of dendritic mitochondria in hippocampal neurons before and after treatment with TTX+APV. N= 14 cells; mean ± SEM; (n.s.) p= 0.060 for midzone fission; **p= 0.0025 for peripheral fission; paired two-tailed t test. **(C)** Quantification of the frequencies of midzone and peripheral fissions of dendritic mitochondria in hippocampal neurons transfected with shRNA-scramble control (SCR) or shRNA-AMPKα2 #1 (AMPKα2 KD). N= 12 cells for SCR, 13 cells for AMPKα2 KD; mean ± SEM; *p= 0.028 for midzone fission; **p= 0.0020 for peripheral fission; unpaired two-tailed t test. **(D, E)** Immunofluorescence of autophagy marker p62 in dendrites of hippocampal neurons expressing shRNA-scramble control (SCR) or shRNA-AMPKα2 (AMPKα2 KD). Cells were labeled with GFP and mito-DsRed. Yellow lines indicate the outlines of dendrites (D). Higher magnified views and surface rendering images of mitochondria (magenta) and p62 puncta (green) in control and AMPKα2 KD cells (E). **(F)** Quantification of the number of p62 puncta in SCR and AMPKα2 KD cells. The number of p62 puncta was divided by the dendritic area. N= 40 cells for SCR, 31 cells for AMPKα2; ***p= 2.9×10^{-7}; Wilcoxon rank-sum test. **(G)** Quantification of the co-localization (Manders overlap coefficient) of p62 puncta and mitochondrial area in SCR and AMPKα2 KD cells. N= 40 cells for SCR, 31 cells for AMPKα2; ***p= 2.1×10^{-7}; Wilcoxon rank-sum test. Box plots denote the median (50th percentile) and the 25th to 75th percentiles of datasets in (F, G). Samples were taken from three independent experiments. Scale bars: 1 μm in (A, E), 5 μm in (D).

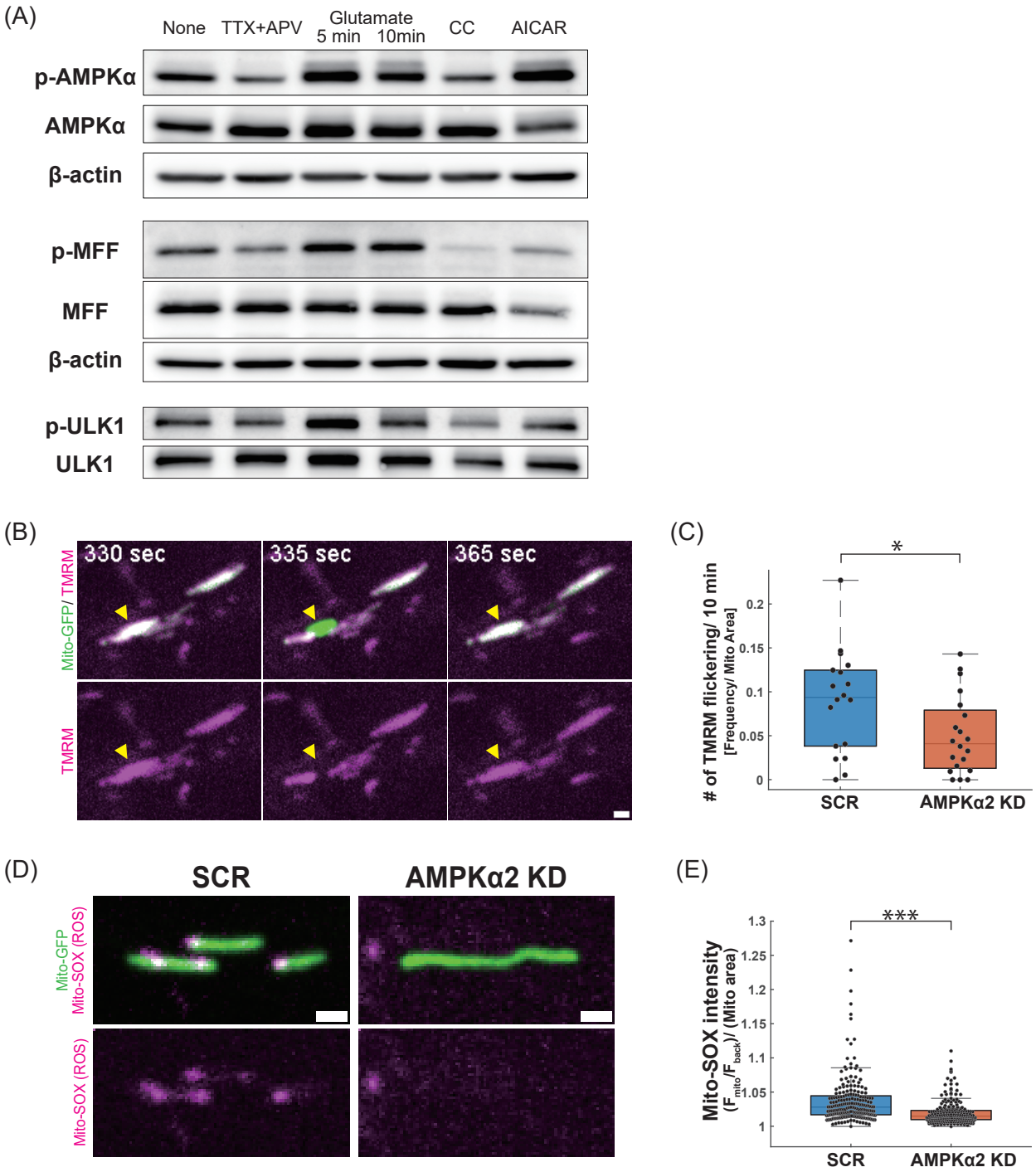

Figure 6. AMPK phosphorylates mitochondrial fission factor (MFF) and ULK1 in response to neuronal activity. **(A)** Phosphorylation of AMPKα and its downstream effectors in neurons treated with either TTX+APV (6h), 100 μM glutamate (5 and 10 min), 20 μM Compound C (CC, 6h) or 2 mM AICAR (6h) at DIV5. Blots were probed with antibodies against total and p-Thr172 AMPKα, total and p-Ser146 MFF, total and p-Ser555 ULK1 and β-actin. Similar results were obtained from three independent cultures. **(B)** Time-lapse images of TMRM flickering in dendritic mitochondria in hippocampal neurons. Cells were transfected with mito-GFP and SCR or AMPKα2 shRNA and treated with 20 nM TMRM. Transient loss of TMRM fluorescence in a single mitochondrion is seen (yellow arrowheads) (see also Supplementary Video 5). **(C)** Quantification of the frequencies of TMRM flickering in control and AMPKα2 KD cells. N= 18 cells for SCR, 20 cells for AMPKα2 KD. Samples were taken from four independent experiments. *p= 0.041, Wilcoxon rank-sum test. **(D)** Mito-SOX signals in dendritic mitochondria in control and AMPKα2 KD cells. Cells were transfected with mito-GFP and SCR or AMPKα2 shRNA and treated with 500 nM Mito-SOX. **(E)** Quantification of the Mito-SOX intensity in individual mitochondria. N= 212 mitochondria from 13 cells for SCR, 225 mitochondria from 17 cells for AMPKα2 KD. Samples were taken from two independent experiments. ***p= 6.9×10^{-15}, Wilcoxon rank-sum test. Box plots denote the median (50th percentile) and the 25th to 75th percentiles of datasets in (C, E). Scale bars: 1 μm in (B, D).

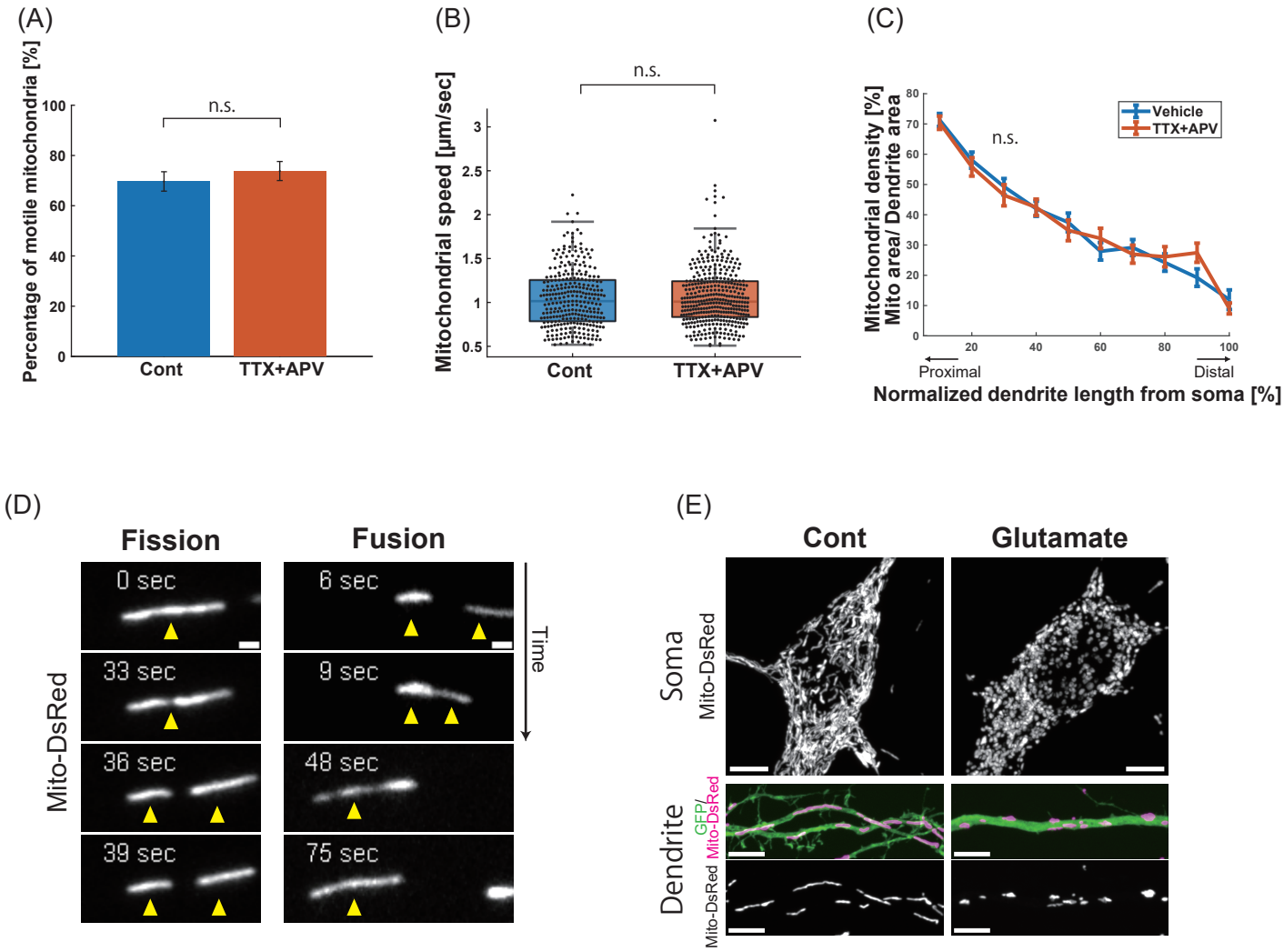

Extended Data Figure 1. Neuronal activity regulates mitochondrial dynamics.

(A) Motile fraction of mitochondria in dendrites before and after TTX+APV treatment. Cells were labeled with mito-DsRed and GFP. N= 14 cells, mean ± SEM, (n.s.) p= 0.45, unpaired two-tailed t test. **(B)** Mitochondrial speed before and after TTX+APV treatment. N= 294 events from 14 control cells, 376 events from 14 drug-treated cells, (n.s.) p= 0.52, Wilcoxon rank-sum test. **(C)** Mitochondrial distribution along the shaft of primary dendrites. The primary dendrites were compartmentalized by the relative length from the soma, with the tip of the dendrite as 100%. Hippocampal neurons expressing GFP and mito-DsRed were treated with vehicle or TTX+APV for 2 days from DIV3 and fixed at DIV5. Mitochondrial density was calculated by dividing the mitochondrial area (demarcated by mitoDsRed) by the dendritic area (demarcated by GFP). N= 23 control cells, 30 drug-treated cells, (n.s.) p> 0.05, unpaired two-tailed t test. **(D)** Time-lapse images of fission and fusion of dendritic mitochondria in hippocampal neurons labeled with GFP and mito-DsRed (see also Supplementary Video 3). **(E)** Mitochondrial morphology in soma and dendrites after 1-min treatment with vehicle or 100 µM Glutamate at DIV6. Scale bars: 1 µm in (D); 5 µm in (E). Samples were taken from three independent experiments.

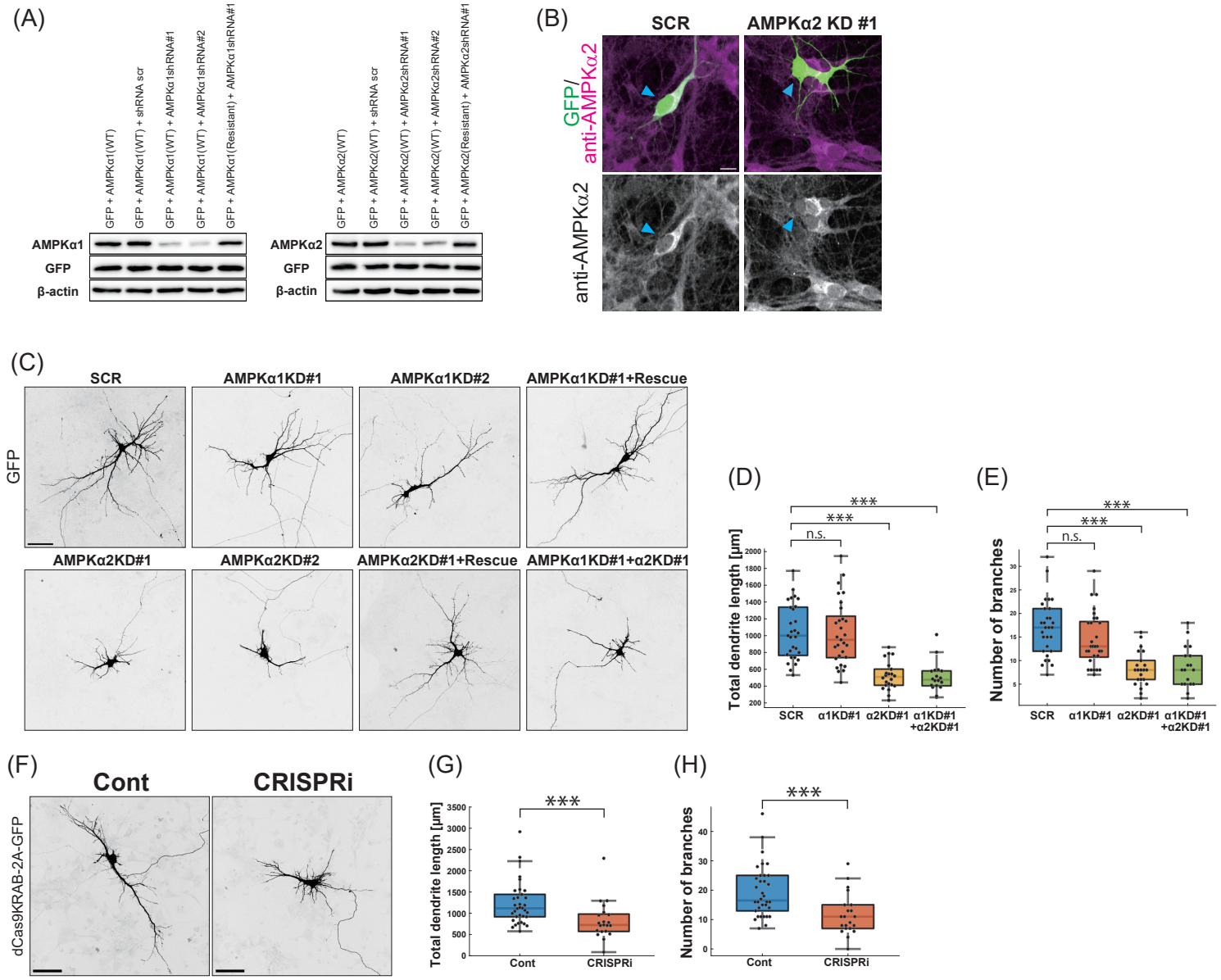

Extended Data Figure 2. Validation of shRNA targeting AMPKα subunits.

(A) HEK293T cells were transfected with GFP and AMPKα1 or AMPKα2 cDNA plasmids with or without respective shRNA constructs. Cell lysates were prepared 2 days after transfection and analyzed by western blotting with antibodies against GFP, AMPKα1, AMPKα2 and β-actin. **(B)** DIV5 hippocampal neurons transfected with GFP and shRNA for the scrambled control (SCR) or AMPKα2 (α2 KD #1) were immunostained with an antibody against AMPKα2. Arrowheads indicate shRNA-transfected neurons. **(C)** Representative images of DIV5 hippocampal neurons transfected with GFP and shRNA for the scrambled control (SCR), AMPKα1 (α1 KD #1 or #2), AMPKα2 (α2 KD #1 or #2), AMPKα1 and α2 (α1KD #1 + α2KD #1), or AMPKα1 (α1 KD #1) or AMPKα2 (α2 KD #1) together with the respective shRNA-resistant mutants (Rescue). **(D, E)** Quantification of total dendritic length (D) and number of branch points (E) of hippocampal neurons described in (C). N= 29 cells for SCR, 29 cells for α1 KD #1, 22 cells for α2 KD #1 from three independent experiments, and 18 cells for α1KD #1 + α2KD #1 from two independent experiments; ***$p<0.001$; (n.s.) $p> 0.05$; Kruskal–Wallis test with Bonferroni multiple comparisons test. **(F)** Morphology of hippocampal neurons transfected with CRISPR interference plasmids for gRNA-empty control (Cont) or gRNA-AMPKα2 (AMPKα2 CRISPRi). Cells were transfected at DIV2 and fixed at DIV5. **(G, H)** Quantification of total dendritic length (G) and number of branch points (H) of neurons described in (F). N= 34 cells for control, 21 cells for AMPKα2 CRISPRi from three independent experiments. ***$p= 9.7\times10^{-4}$ (G), ***$p= 6.4\times10^{-4}$ (H), Wilcoxon rank-sum test. Box plots denote the median (50th percentile) and the 25th to 75th percentiles of datasets in (D, E, G, H). Scale bars: 10μm in (B), 50 μm in (C, F).

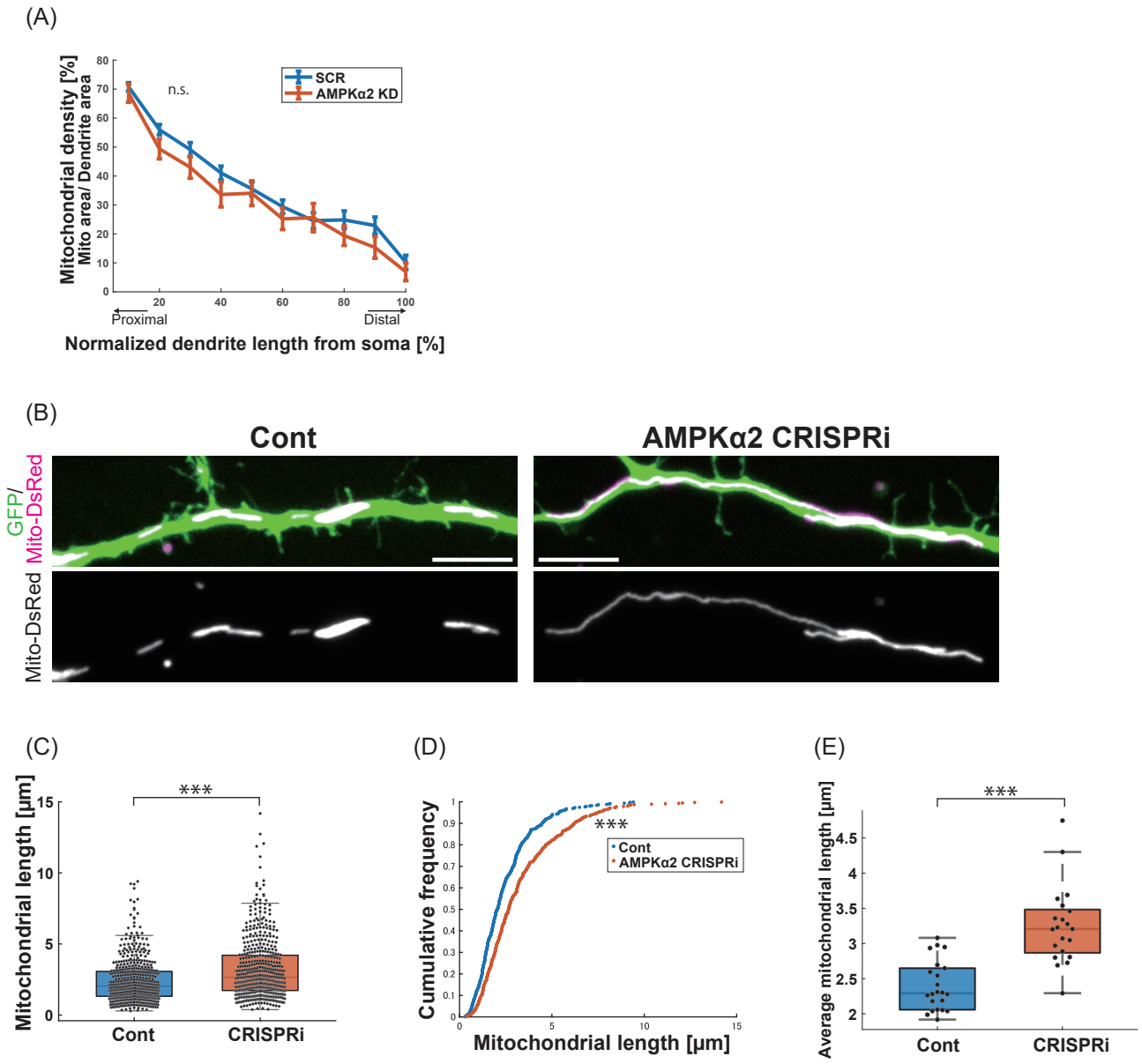

Extended Data Figure 3. AMPK induces mitochondrial fission in dendrites of growing hippocampal neurons. **(A)** Mitochondrial distribution along the shaft of primary dendrites. Hippocampal neurons were transfected with GFP, mito-DsRed and shRNA-scramble control (SCR) or shRNA-AMPKα2 (AMPKα2 KD) at DIV3 and fixed at DIV5. The primary dendrites were compartmentalized by the relative length from the soma, with the tip of dendrite defined as 100%. The mitochondrial density was calculated by dividing the mitochondrial area (demarcated by mitoDsRed) by the dendritic area (demarcated by GFP). N= 22 cells for SCR, 24 cells for AMPKα2 KD; (n.s.) $p > 0.05$; unpaired two-tailed t test. **(B)** Morphology of dendritic mitochondria in hippocampal neurons transfected at DIV2 with CRISPR interference plasmids for gRNA-empty control (Cont) or gRNA-AMPKα2 (AMPKα2 CRISPRi) and fixed at DIV5. Cells were labeled with mito-DsRed and GFP. Scale bars: 5 μm. **(C, D)** Distribution (C) and cumulative frequency (D) of the mitochondrial length in dendrites. N= 534 mitochondria from 22 control cells, 497 mitochondria from 21 CRISPRi cells; *** $p = 8.0\times10^{-12}$; Wilcoxon rank-sum test. **(E)** Average mitochondrial length in individual cells. N=22 cells for control, 21 cells for CRISPRi; *** $p = 2.3\times10^{-6}$; Wilcoxon rank-sum test. Box plots denote the median (50th percentile) and the 25th to 75th percentiles of datasets in (C, E). Samples were taken from three independent experiments.

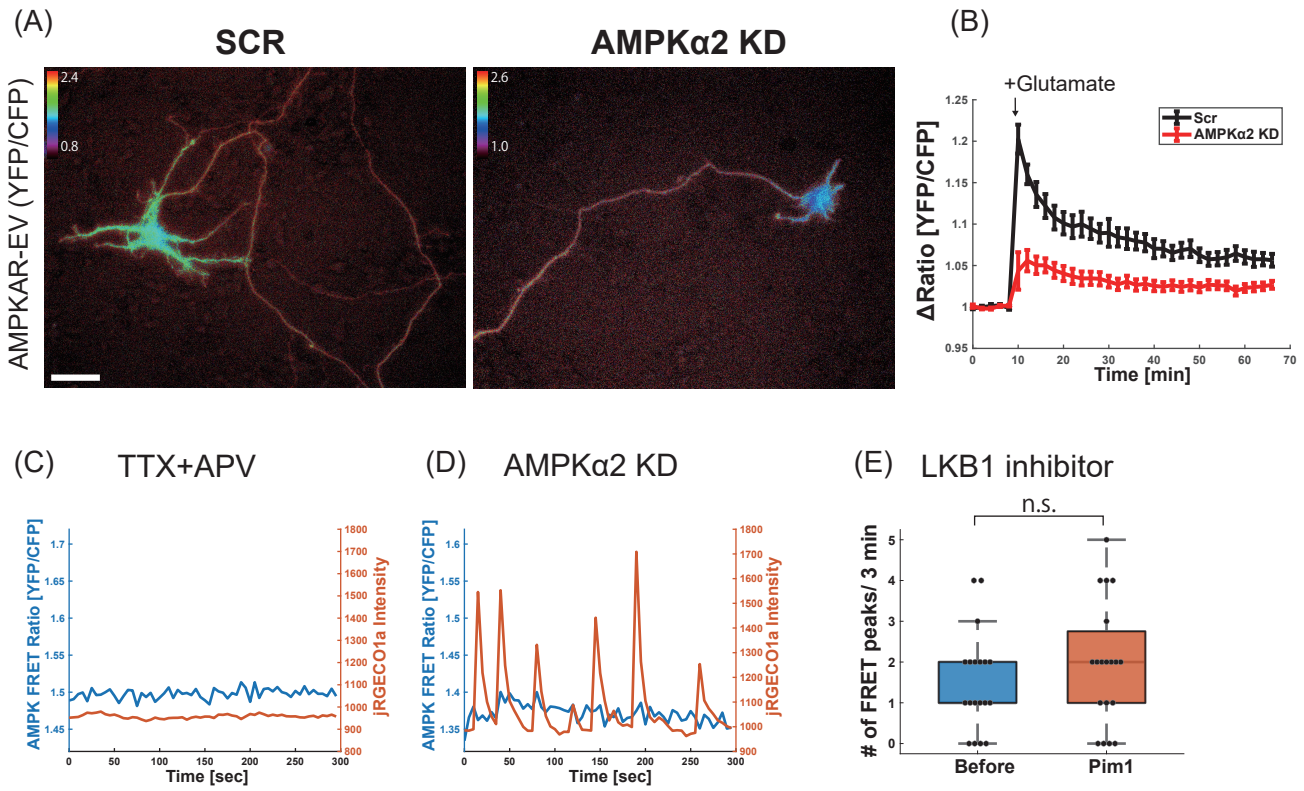

Extended Data Figure 4. AMPK activity in hippocampal neurons visualized by AMPKAR-EV. **(A)** Subcellular distribution of AMPKAR-EV FRET signals in hippocampal neurons at DIV5. Cells were transfected with AMPKAR-EV together with shRNA-scramble control (SCR) or shRNA-AMPKα2 (AMPKα2 KD). Scale bar: 50 μm. **(B)** Activation of AMPK induced by neuronal activity. DIV5 hippocampal neurons expressing AMPKAR-EV with shRNA-scramble control (SCR) or shRNA-AMPKα2 #1 (AMPKα2 KD) were treated with 1 μM glutamate. The YFP/CFP ratio in dendrites was monitored every 2 min for 70 min before and after glutamate treatment. N= 18 cells for control and AMPKα2 from two independent experiments. **(C)** Representative traces of AMPK activity and Ca^{2+} influx in hippocampal neurons treated with TTX+APV. Cells were transfected with AMPKAR-EV and jRGECO1a. **(D)** Representative traces of AMPK activity and Ca^{2+} influx in hippocampal neurons transfected with AMPKAR-EV, jRGECO1a and shRNA-AMPKα2. **(E)** Quantification of the frequency of AMPKAR-EV FRET peaks in hippocampal neurons expressing AMPKAR-EV before and after treatment with 1 μM Pim1 (LKB1 inhibitor) at DIV5. N= 19 cells from two independent experiments, (n.s.) p= 0.30, Wilcoxon signed-rank test. Box plots denote the median (50th percentile) and the 25th to 75th percentiles of datasets.

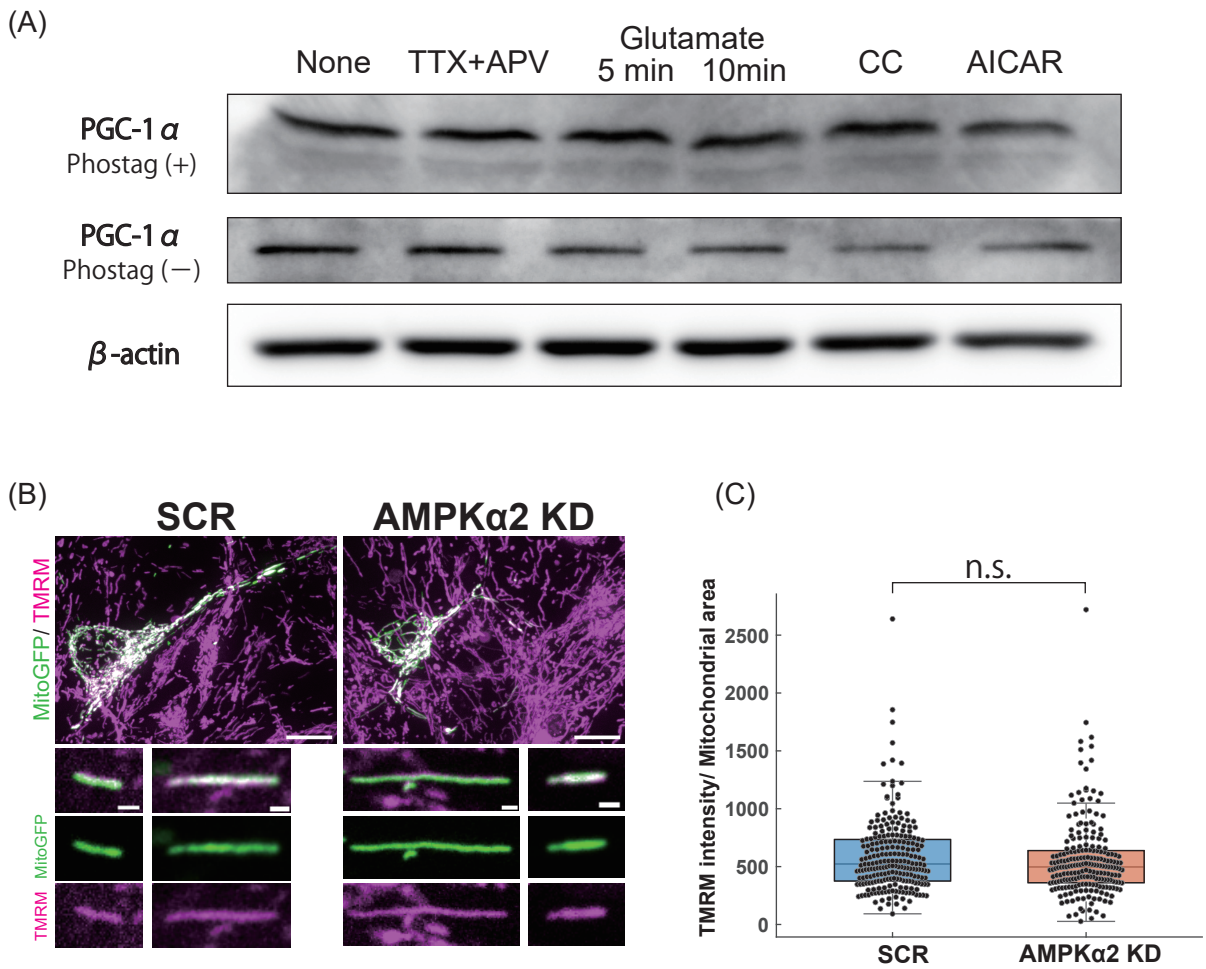

Extended Data Figure 5. Effects of AMPK deficiency on PGC1α phosphorylation and mitochondrial membrane potential.

(A) Phos-tag SDS-PAGE for a mitochondrial biogenesis marker, PGC1α in neurons treated with either TTX+APV (6h), 100 μM glutamate (5 or 10 min), 20 μM Compound C (CC, 6h), or 2 mM AICAR (6h). Cell lysates were subjected to Phos-tag SDS-PAGE (100 μM Phos-tag) and standard SDS-PAGE, followed by immunoblotting with antibodies for PGC1α and β-actin. **(B)** Representative images of dendritic mitochondria in neurons treated with 20 nM TMRM (magenta). Cells were transfected with mito-GFP (green) together with shRNA-scramble control (SCR) or shRNA-AMPKα2 (AMPKα2 KD). **(C)** Quantification of TMRM intensity in individual mitochondria. N= 227 mitochondria from 17 control cells, 216 mitochondria from 15 AMPKα2 KD cells from two independent experiments. (n.s.) p= 0.14, Wilcoxon rank-sum test. Box plots denote the median (50th percentile) and the 25th to 75th percentiles of datasets. Scale bars: 10 μm (B, upper panels), 1 μm (B, lower panels).

Supplementary information

Supplementary Video 1. Calcium transients in hippocampal neurons before and after TTX+APV treatment. Cells were transfected with GCAMP6s at DIV3. Images were acquired every 3 sec for 5 min at DIV5 using spinning disk confocal microscopy. Display rate: 10 frames/second. Scale bar: 10 μm. Related to Fig. 1A.

Supplementary Video2. Time-lapse movies of growing hippocampal neurons cultured in the presence or absence of TTX+APV. Cells were labeled with GFP. Images were acquired every 30 min for 52 h from DIV5 to 7 using spinning disk confocal microscopy. Display rate:10 frames/second. Scale bar: 50 μm. Related to Fig. 1B.

Supplementary Video3. Time-lapse movies of mitochondrial fission and fusion in dendrites
Cells were labeled with mito-DsRed and GFP. Time-lapse images were acquired every 3 sec for 20 min at DIV5 using spinning disk confocal microscopy. Display rate: 8 frames/second. Scale bar: 1 μm. Related to Extended Data Fig. 1D.

Supplementary Video 4. Simultaneous imaging of AMPK activity and Ca^{2+} transients before and after TTX+APV treatment.
Cultured hippocampal neurons were transfected with AMPKAR-EV and jRGECO1a. The pseudo-color represents the YFP/CFP ratio (AMPK activity, left), and the Ca^{2+} influx (right), respectively. Images were acquired every 5 sec for 5 min at DIV5 using epifluorescence microscopy. Display rate: 5 frames/second. Scale bar: 10 μm. Related to Fig. 4E-G.

Supplementary Video 5. Time-lapse movie of mitochondrial TMRM flickering.
Cultured hippocampal neurons transfected with mito-GFP (green) were treated with 20 nM TMRM (magenta) at DIV5. Images were acquired every 5 sec for 10 min using spinning disk confocal microscopy. Display rate: 8 frames/ second. Scale bar: 1 μm. Related to Fig. 6B.